University of Helsinki Report Series in Physics

HU-P-D258

Infrared Behavior of SU(2) Gauge Theory

Viljami Leino

Department of Physics
Faculty of Science
University of Helsinki

ACADEMIC DISSERTATION

To be presented, with the permission of the Faculty of Science of the University of Helsinki, for public criticism in the auditorium CK112 at Exactum, Gustaf Hällströmin katu 2 B, on Thursday 16th of August 2018 at 12 o'clock

Helsinki 2018

Supervisors:
Prof. Kari Rummukainen
University of Helsinki

Dr. Kimmo Tuominen
University of Helsinki

Pre-examiners:
Prof. Claudio Pica
CP^3-Origins, University of Southern Denmark

Prof. Tuomas Lappi
University of Jyväskylä

Opponent:
Assoc. Prof. Stefan Sint
Trinity College Dublin

Custos:
Prof. Kari Rummukainen
University of Helsinki

ISBN 978-951-51-2783-9 (printed version)
ISBN 978-951-51-2784-6 (pdf)
ISSN 0356-0961
http://ethesis.helsinki.fi
Helsinki 2018
Unigrafia

Abstract

The Standard Model of particle physics provides the most precise description of elementary particle physics. However, the Standard Model is not a complete theory and many theoretical questions still remain unanswered. For example, the exact nature of dark matter, baryogenesis, and neutrino masses remain unknown. Therefore, there is still need for beyond the Standard Model physics.

Many interesting beyond the Standard Model scenarios rely on strong interactions. For example, the extended technicolor mechanism could explain the fermion masses and the electroweak symmetry breaking without elementary scalar fields. However, perturbative calculations at large couplings are not reliable and non-perturbative methods are needed. Of special interest are theories which have a vacuum phase structure indicating an existence of an infrared fixed point. Such conformal theories form a basic building block of many beyond the Standard Model scenarios, including the aforementioned extended technicolor theory.

In this thesis I present the results of multiple studies aiming to understand the infrared behavior and conformal window of the $SU(2)$ gauge model with six and eight massless Dirac fermions transforming in the fundamental representation of the gauge group. Multiple theoretical estimates indicate that the conformality sets in between five and eight fermions in the $SU(2)$ model, rendering six and eight fermion cases interesting for non-perturbative study. However, previous lattice studies on the six and eight fermion cases have been inconclusive.

Using clover improved fermion action and smeared Wilson gauge action, we have performed a gradient flow study of the coupling and scheme invariant quantities: the mass anomalous dimension γ_m and the leading irrelevant exponent of the coupling γ_g. Our results indicate that both of the models under the study have infrared fixed points and are therefore within the conformal window.

Tiivistelmä

Vuonna 2012 CERN:ssä Large Hadron Collider (LHC) hiukkaskiihdyttimellä kokeellisesti varmistettu Higgsin hiukkanen oli viimeinen havaitsematon osa hiukkasfysiikan standardimallia. Hiukkasfysiikan standardimalli on äärimmäisen tarkka kuvaus aineen rakenteesta suurilla energioilla. Se ei kuitenkaan selitä kaikkea tunnettua fysiikkaa. Aiheet kuten gravitaatio, pimeä aine, baryogeneesi ja neutriinoiden massat ovat nykyisen standardimallin selityskyvyn ulkopuolella.

Osa standardimallin jälkeisistä teorioista vaatii vahvasti vuorovaikuttavan aineen ymmärtämistä. Esimerkkinä tämänkaltaisesta teoriasta toimii tekniväri, joka pyrkii selittämään sähköheikon symmetriarikon ja fermionien massat tekemällä Higgsin hiukkasesta yhdistelmähiukkasen. Tämä värineutraali yhdistelmähiukkanen koostuisi teknikvarkeista. Jotta tekniväriteorioiden ennusteet sopisivat nykyisiin mittaustuloksiin, on niiden kytkinvakion kehityttävä hitaasti energian muuttuessa. Tätä käytöstä kutsutaan kytkimen kävelemiseksi.

Kävelevien teorioiden löytämisen helpottamiseksi, voidaan jokaiselle värimäärälle löytää fermionimäärä jolla teorian kytkinvakio ei kehity ollenkaan infrapunakiintopisteen takia. Tämän konformi-ikkunaksi kutsutun alueen alarajan löytäminen kahden värin teoriassa on tämän väitöskirjan aihe. Erityisesti tutkimuksen kohteena ovat kuuden ja kahdeksan fermionin tapaukset, sillä neljän fermionin tapauksen tiedetään olevan konformi-ikkunan ulkopuolella ja kymmenen fermionin tapauksen olevan konformi-ikkunan sisällä.

Tutkimus on toteutettu hilasimulaatioina supertietokoneilla ja simulaatioteknisistä syistä tutkimus keskittyy parillisiin fermionimääriin. Löydämme infrapunakiintopisteen sekä kuuden että kahdeksan fermionin tapauksissa ja toteamme näiden mallien olevan konformi-ikkunan sisällä. Esitämme myös tulokset kahdelle muulle infrapunasuureelle: massan anomaaliselle eksponentille ja kytkinvakion johtavalle epäoleelliselle eksponentille.

Acknowledgments

First and foremost I would like to thank my supervisors Kari Rummukainen and Kimmo Tuominen for their invaluable guidance and support throughout my time as graduate student. I would also like to thank my collaborators Jarno Rantaharju, Teemu Rantalaiho, Joni Suorsa and Sara Tähtinen for the fruitful discussions and their contributions to the research done for this thesis.

I am grateful for Claudio Pica and Tuomas Lappi for their valuable comments and corrections on the manuscript of this thesis. I would like to thank Stefan Sint for agreeing to be my opponent. I am also grateful for Oleg Lebedev and Aleksi Vuorinen who agreed to be in the grade committee.

The department of physics in University of Helsinki and the Helsinki institute of physics have provided a cheerful environment for the research. I especially want to thank all the members of the computational field theory group, and all my fellow doctoral students for insightful discussions.

I acknowledge the financial support granted by the Jenny and Antti Wihuri foundation. The simulations for this research were done in the supercomputers at: the CSC in Espoo, Finland, and the CINECA in Bologna, Italy.

Finally, I would like to thank my family and friends for their continuous support and encouragement.

Helsinki, August 2018

Viljami Leino

List of publications

I. V. Leino, J. Rantaharju, T. Rantalaiho, K. Rummukainen, J. M. Suorsa, and K. Tuominen,
Gradient flow running coupling in SU(2) gauge theory with $N_f = 8$ fundamental flavors,
Phys. Rev. D **95** (Jun, 2017) 114516, [arXiv:1701.04666].

II. V. Leino, K. Rummukainen, J. M. Suorsa, K. Tuominen, and S. Tähtinen,
Infrared fixed point of SU(2) gauge theory with six flavors,
Phys. Rev. D **97** (Jun, 2018) 114501, [arXiv:1707.04722].

III. V. Leino, K. Rummukainen, and K. Tuominen,
Slope of the beta function at the fixed point of SU(2) gauge theory with six or eight flavors,
Submitted to PRD (2018) [arXiv:1804.02319].

Author's contributions

I. The author did most of the simulations and the final analysis of the running of the coupling. The author also measured the mass anomalous dimension using the Schrödinger functional step scaling method.

II. The author did all the simulations and did the data analysis of the running of the coupling. The author also measured the mass anomalous dimension using the Schrödinger functional step scaling method.

III. The author did all of the data analysis.

All papers were jointly written by all of the authors.

Contents

Chapter 1

Beyond the Standard Model

1.1 The Standard Model

The most precise model of modern particle physics is the Standard Model (SM). The Standard Model combines the theory of electroweak interaction with the theory of quantum chromodynamics (QCD) into a one renormalizable theory. This theory explains three of the four fundamental interactions of nature, excluding only gravity. After the discovery of the Higgs particle in 2012 at the Large Hadron collider [4, 5], all Standard Model particles have been experimentally verified and are listed in figure 1.1 together with their quantum numbers [6].

The Standard Model has the gauge symmetry $SU(3)_C \times SU(2)_I \times U(1)_Y$, where the $SU(3)_C$ part describes quantum chromodynamics. QCD is a strongly interacting theory that has color as a conserved charge. The color charge is mediated by eight bosonic gluons g [7, 8]. The gluons interact with themselves and only with the six fermionic quarks [9–11] that have been named: up, down, strange, charm, top, and bottom. The quarks are organized into three families of up type quarks, with electric charge $Q = \frac{2}{3}$, and down type quarks, with $Q = -\frac{1}{3}$. However, neither quarks or gluons can be observed as free particles, because the theory of QCD is confining. This confining property is a consequence of the asymptotic freedom. With asymptotic freedom, the strength of the strong interaction increases at long distances (or small energies), which confines the quarks and gluons into composite particles. These composite particles are called hadrons.

The $SU(2)_I \times U(1)_Y$ part of the symmetry corresponds to the electroweak force [12] with weak isospin and hypercharge as conserved charges. However, the Higgs mechanism [13, 14], caused by the Higgs particle, spontaneously breaks this symmetry to a $U(1)_{\text{em}}$ symmetry, and divides the theory to weak and elec-

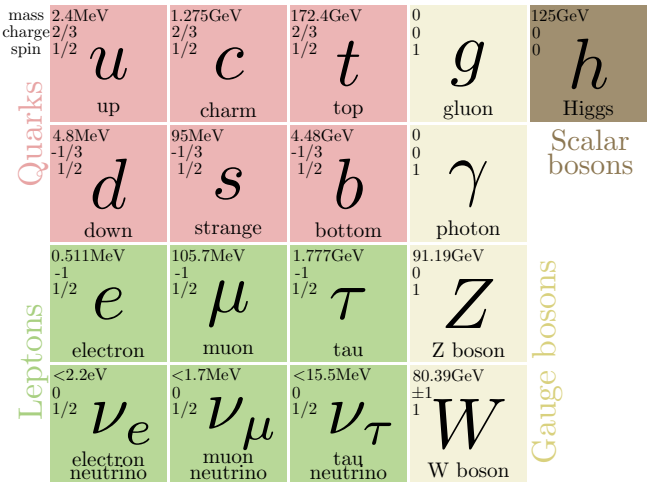

Figure 1.1: Particles included in the Standard model.

tromagnetic interactions. The electroweak theory has three gauge bosons: the W and Z bosons mediate the weak interaction and the photon γ mediates the electromagnetic interaction. The photon is massless, while the weak gauge bosons are massive, because they absorb the Goldstone bosons created in the symmetry breaking process. Apart from the gauge bosons, the electroweak interaction affects the three generations of fermions called the leptons. These three lepton generations come with the associated three generations of neutrinos. In the Standard Model the neutrinos are assumed to be massless. However, there are experimental results indicating that neutrinos have tiny masses.

We will now proceed to give more detailed explanation of the Standard Model. Firstly, the three generations of quarks and leptons come in left and right handed varieties. The handedness is related to the chirality of the particle and can be defined with the left and right handed projections:

$$\psi_L = P_L\psi = \frac{1-\gamma_5}{2}\psi\,, \quad \psi_R = P_R\psi = \frac{1+\gamma_5}{2}\psi\,, \tag{1.1}$$

where γ_5 is the chirality matrix that anticommutes with the Dirac matrices γ_μ, and ψ is the fermion field. The weak interaction couples only to the left handed fermions, which causes the fermions to organize so that the left handed particles form a $SU(2)_L$ doublet under the weak isospin, while the right handed particles are represented as $SU(2)_R$ singlets. The only exception to this rule are the neutrinos that are always left handed. This asymmetry between left and right handed particles leads to parity violation. We present the division to left and right handed

fermions in a matrix form as:

$$Q_L = \begin{pmatrix} u_L \\ d_L \end{pmatrix}, \quad E_L = \begin{pmatrix} (\nu_e)_L \\ e_L^- \end{pmatrix}, \quad u_R, \quad d_R, \quad \text{and} \quad e_R^-. \tag{1.2}$$

In this notation, we can express the Standard Model Lagrangian for a single family of particles as:

$$\mathcal{L}_{\text{SM}} = \mathcal{L}_{\text{gauge}} + \mathcal{L}_{\text{kinetic}} + \mathcal{L}_{\text{Yukawa}} + \mathcal{L}_{\text{Higgs}} \tag{1.3}$$

$$\mathcal{L}_{\text{gauge}} = -\frac{1}{4} F^a_{\mu\nu} F_a^{\mu\nu} - \frac{1}{4} W^a_{\mu\nu} W_a^{\mu\nu} - \frac{1}{4} B_{\mu\nu} B^{\mu\nu} \tag{1.4}$$

$$\mathcal{L}_{\text{kinetic}} = \bar{Q}_L \left(i\not{D}\right) Q_L + \bar{E}_L \left(i\not{D}'\right) E_L + \bar{u}_R \left(i\not{D}\right) u_R + \bar{d}_R \left(i\not{D}\right) d_R + \bar{e}_R \left(i\not{D}'\right) e_R \tag{1.5}$$

$$\mathcal{L}_{\text{Yukawa}} = -\lambda_u \bar{Q}_L \phi u_R - \lambda_d \bar{Q}_L \phi d_R - \lambda_l \bar{E}_L \phi e_R \tag{1.6}$$

$$\mathcal{L}_{\text{Higgs}} = \left| D'_\mu \phi \right|^2 - \mu^2 \phi^\dagger \phi - \lambda (\phi^\dagger \phi)^2 , \tag{1.7}$$

where

$$D_\mu = \partial_\mu - i g_f B_\mu - i g' \sigma \cdot W_\mu - i g \tau \cdot A_\mu \tag{1.8}$$

$$D'_\mu = \partial_\mu - i g_f B_\mu - i g' \sigma \cdot W_\mu \tag{1.9}$$

$$F^a_{\mu\nu} = -i[D^{ac}_\mu, D^{cb}_\nu] = \partial_\mu A^a_\nu - \partial_\nu A^a_\mu + g f^{abc} A^a A^b \tag{1.10}$$

$$W^a_{\mu\nu} = \partial_\mu W^a_\nu - \partial_\nu W^a_\mu + g' \epsilon^{abc} W^a W^b \tag{1.11}$$

$$B_{\mu\nu} = \partial_\mu B_\nu - \partial_\nu B_\mu , \tag{1.12}$$

where f_{abc} and ϵ_{abc} are the structure constants, $[\cdot, \cdot]$ is the commutator, $\not{D} = \gamma^\mu D_\mu$, and τ and σ are the generators of $SU(3)$ and $SU(2)$ respectively and are indexed by a.

The term $\mathcal{L}_{\text{gauge}}$ encodes the gauge invariant kinetic terms of the gauge fields. The self-interactions of the non-Abelian gauge fields, with gauge couplings g and g', are generated by the structure constants in the field strengths $F_{\mu\nu}$ and $W_{\mu\nu}$.

The term $\mathcal{L}_{\text{kinetic}}$ encodes the interaction between gauge bosons and fermions. All the fermions receive masses through their interactions with the Higgs boson, which is described by the Yukawa terms in the term $\mathcal{L}_{\text{Yukawa}}$. The masses have to be encoded in the Yukawa term, since adding the masses traditionally as a term: $m\bar{\psi}\psi = m\bar{\psi}_R \psi_L + \bar{\psi}_L \psi_R$, would break the gauge symmetry by mixing left- and right handed particles, which transform differently under the weak $SU(2)$. The Yukawa terms solve this discrepancy by replacing the masses with weak isospin doublets of a scalar field ϕ, which restores the gauge symmetry. Apart from the fermion masses, the Higgs field is also responsible of the weak gauge boson masses, through the Higgs mechanism in the term $\mathcal{L}_{\text{Higgs}}$. The description of the Higgs mechanism is left to section 1.2.

1.2 Electroweak symmetry breaking

The masses of fermions and weak gauge bosons are generated through the Higgs mechanism. To understand the spontaneous breaking of the electroweak symmetry, we look at the complex scalar potential in the term $\mathcal{L}_{\text{Higgs}}$ which encodes the self-interaction of the Higgs field ϕ:

$$V(\phi) = \mu^2\phi^\dagger\phi + \lambda(\phi^\dagger\phi)^2\,, \tag{1.13}$$

where $\mu^2 < 0$ and $\lambda > 0$ are free parameters and the scalar field ϕ is chosen to be a $SU(2)$ doublet in order to satisfy the $SU(2) \times U(1)$ gauge symmetry:

$$\phi = \begin{pmatrix} \phi^+ \\ \phi^0 \end{pmatrix}\,. \tag{1.14}$$

The potential has a local maximum at $\phi = 0$ and global minima along a circle $|\phi|^2 = -\mu^2/2\lambda = \nu^2$. As the field chooses a particular ground state along that circle, the ground state is no longer invariant under $SU(2) \times U(1)$ transformations and hence the symmetry gets spontaneously broken. After the symmetry is broken, the $U(1)_{\text{em}}$ remains a gauge symmetry of the system.

The Goldstone theorem [15] states that for every generator of a broken symmetry, a massless Goldstone boson will be generated. Since the electroweak symmetry had three generators, there will be three Goldstone bosons. By choosing unitary gauge, the Goldstone bosons become the longitudinal polarizations of the weak gauge bosons.

In the unitary gauge, the scalar field can be expanded around the vacuum expectation value with respect to fluctuations $h(x)$ as:

$$\phi = \frac{1}{\sqrt{2}}\begin{pmatrix} 0 \\ \nu + h(x) \end{pmatrix}\,. \tag{1.15}$$

Moreover, the Higgs Lagrangian from Eq. (1.7) can now be written as:

$$\mathcal{L}_{\text{Higgs}} = \left(1+\frac{h}{\nu}\right)\left[M_W^2 W_\mu^\dagger W^\mu + \frac{1}{2}M_Z^2 Z_\mu Z^\mu\right] + \frac{1}{2}\partial_\mu h \partial^\mu h - \frac{1}{2}M_h h^2 - \frac{M_H^2}{2\nu}h^3 - \frac{M_h^2}{8\nu^2}h^4, \tag{1.16}$$

where the mass of the W boson is related to the mass of the Z boson through weak mixing angle θ_w as:

$$M_W = M_Z \cos\theta_W = M_Z \frac{g'}{\sqrt{g'^2 + g_f^2}} = g\nu/2\,. \tag{1.17}$$

Written in this form, the term $\mathcal{L}_{\text{Higgs}}$ has mass terms for the weak gauge bosons as well as the Higgs self-interaction term. It also encodes the interactions between the weak gauge bosons and the Higgs particle.

The fermion masses are generated through the Yukawa couplings in the Lagrangian $\mathcal{L}_{\text{Yukawa}}$ (1.6). Expanding the scalar fields with Eq. (1.15) the Yukawa terms become:

$$\mathcal{L}_{\text{Yukawa}} = \left(1 + \frac{h}{\nu}\right)\left[m_u \bar{u}u + m_d \bar{d}d + m_e \bar{e}e\right] , \tag{1.18}$$

where $m_i = \lambda_i \nu/\sqrt{2}$. Therefore electroweak symmetry breaking generates the fermion masses. The free parameters λ_i are arbitrary and have to be fixed to match the measured masses.

1.3 Symmetries of QCD

QCD has several interesting symmetries. In order to study these symmetries, we explicitly add fermion mass terms to the Lagrangian density, which simplifies the discussion:

$$\mathcal{L}_{\text{QCD}} = \bar{\psi}\left(i\not{D} - m\right)\psi - \frac{1}{4}F_{\mu\nu}F^{\mu\nu} , \tag{1.19}$$

where $\not{D}$ and m are diagonal matrices with size proportional to the number of fermions N_f. The quark field ψ is a vector in $N_c = 3$ color space and symmetric under gauge $SU(N_c)$ transformations:

$$\psi \to V\psi , \quad \bar{\psi} \to \bar{\psi}V^\dagger , \quad A_\mu \to V\left(\partial_\mu + A_\mu\right)V^\dagger , \quad D_\mu\psi \to V D_\mu \psi , \tag{1.20}$$

where $V = \exp(i\theta \cdot \tau)$, ,$A_\mu$ is the gauge field, and τ is a vector consisting of the $N_c^2 - 1$ generators τ^a of the color Lie algebra.

Apart from the color gauge symmetry, QCD is invariant under Lorentz transformations and has three discrete symmetries: parity transformation $(x_0, x_i) \to (x_0, -x_i)$, time reversal $(x_0, x_i) \to (-x_0, x_i)$, and charge conjugation $\psi \to C\bar{\psi}^{\text{T}}$. with C being the charge conjugation matrix. The QCD action is invariant under the product of the symmetries CPT, which is experimentally verified feature of the theory [6].

The chiral limit, where the theory is taken to be massless $m \to 0$, reveals some interesting properties of QCD. In the chiral limit the kinetic term can be divided into left- and right parts, similarly to Eq. (1.5): $\mathcal{L}^{\text{QCD}}_{\text{quarks}} = \bar{\psi}(i\not{D})\psi = \bar{\psi}_R(i\not{D})\psi_R + \bar{\psi}_L(i\not{D})\psi_L$, where ψ_R and ψ_L are defined in terms of the chiral projections of Eq. (1.1). The fermionic part of the Lagrangian $\mathcal{L}^{\text{QCD}}_{\text{quarks}}$ is invariant under the

global flavor symmetry: $U_R(N_f) \times U_L(N_f) = SU_R(N_f) \times SU_L(N_f) \times U_R(1) \times U_L(1)$ and transforms with the following rules:

$$\psi_{L/R} \to e^{-i\alpha_{L/R}} e^{-i\theta_{L/R}\cdot\tau} \psi_{L/R}\,, \quad \bar{\psi}_{L/R} \to \bar{\psi}_{L/R} e^{i\alpha_{L/R}} e^{i\theta_{L/R}\cdot\tau}\,, \tag{1.21}$$

where α and θ correspond to $U(1)$ and $SU(N_f)$ transformations respectively. The conserved currents corresponding to these symmetry transformations are:

$$j^{\mu}_{L/R} = \bar{\psi}_{L/R}\gamma^{\mu}\psi_{L/R}\,, \quad j^{\mu,a}_{L/R} = \bar{\psi}_{L/R}\gamma^{\mu}\tau^{a}\psi_{L/R}\,. \tag{1.22}$$

These can be combined to vector currents, which treat left- and right handed particles equivalently, and axial currents, which treat them differently:

$$V^{\mu} = j^{\mu}_{R} + j^{\mu}_{L} = \bar{\psi}\gamma^{\mu}\psi\,, \qquad V^{\mu,a} = j^{\mu,a}_{R} + j^{\mu,a}_{L} = \bar{\psi}\gamma^{\mu}\tau^{a}\psi\,, \tag{1.23}$$

$$A^{\mu} = j^{\mu}_{R} - j^{\mu}_{L} = \bar{\psi}\gamma^{\mu}\gamma^{5}\psi\,, \qquad A^{\mu,a} = j^{\mu,a}_{R} - j^{\mu,a}_{L} = \bar{\psi}\gamma^{\mu}\gamma^{5}\tau^{a}\psi\,. \tag{1.24}$$

The vector- and axial currents factor the symmetry group as: $U_R(N_f) \times U_L(N_f) = SU_V(N_f) \times SU_A(N_f) \times U_V(1) \times U_A(1)$.

The $U_V(1)$ symmetry corresponds to the conservation of baryon number, which is an exact symmetry of QCD. Baryon number is conserved even when the masses are turned back on. On the other hand, $SU_V(N_f)$ corresponds to isospin conservation, which is an approximate symmetry for the full massive QCD. The existence of a mass term does not directly break isospin conservation, but differences between quark masses do. Since none of the quarks have same mass, isospin symmetry is broken. However, the strength of the breaking depends on the number of quarks in the model. For $N_f = 2$ the up and down quarks have different but nearly identical masses and isospin symmetry remains a good approximation. On the contrary, for the full $N_f = 6$, isospin symmetry is completely broken by the mass difference between heavy and light quarks.

As for the axial symmetries, $SU_A(N_f)$ corresponds to conservation of the axial current. However, the QCD vacuum is not invariant under the $SU_A(N_f)$ rotations and the axial $SU_A(N_f)$ symmetry is spontaneously broken. Since the symmetry is spontaneously broken, we will generate a number of massless Goldstone bosons equivalent to the number of generators in $SU(N_f)$, as stated by the Goldstone theorem. Usually, the two or three lightest quarks can be considered massless. In the case of $N_f = 3$, $SU(3)$ has 8 generators corresponding to an octet of pseudoscalar mesons: $K^{-,0,+}$, $\bar{K}^0$, $\pi^{-,0,+}$, and η. Since the chiral limit is merely an approximation in QCD and the quarks have masses, these pseudoscalar mesons also acquire small masses: $m_\pi \sim 138\text{MeV}$, $m_K \sim 495\text{MeV}$, and $m_\eta \sim 548\text{MeV}$. Had we chosen $N_f = 2$ instead, the number of broken generators would have been

three, which would generate a triplet of pions. This explains the mass difference between m_π to both m_K and m_η.

While the mass terms explicitly break the chiral symmetry, the chiral limit is still valid approximation and explains the mass differences between mesons. In this case we call the axial current to be partially conserved (PCAC) [16].

Lastly, $U_A(1)$ is an anomalous symmetry. While the action is symmetric under $U_A(1)$, and it would correspond to conservation of difference of the numbers of right- and left handed quarks, the symmetry is broken by quantum fluctuations. If $U_A(1)$ would not be anomalous, it would also break spontaneously and add one extra Goldstone boson η', but, as this is not the case, η' is not Goldstone boson and has a mass of $m_{\eta'} = 958\text{MeV}$, which is considerably larger than the masses of the pseudoscalar octet.

1.4 Renormalization group

The Lagrangian in Eq. (1.19) is a bare Lagrangian and does not have an explicit dependence on the energy scale. The energy scale comes into the picture, when we inspect physical quantities to beyond the tree level in the perturbation theory. The loop integrals over the virtual off-shell particles will generate divergent contributions to physical observables. In order to handle these divergences, two steps must be taken. First the theory is regularized. The regularization introduces a new parameter μ that modifies the theory in such a way that all quantities become finite. Common regularization methods are the cutoff method and the dimensional regularization [17]. Secondly, the renormalization process applies the renormalization conditions to bare quantities, such as coupling constants, which relates them to physically measurable observables. As long as the theory is renormalizable, there are finite number of such renormalization steps. At the end of the renormalization process, we will have physical quantities free of divergences given at different energy scales μ. The renormalization process can be done in a multiple different ways, called the renormalization schemes, that will all lead to same physical observables.

The way the theory changes when μ is changed is encoded in the renormalization group. In order to find a mathematical formulation for the renormalization group, we will look at the connected n-point function of quark fields q at a scale μ: $G^n(q, \bar{q}, m, g, \mu)$. Assuming multiplicative renormalization, G^n is given in terms of bare n-point function G_0^n by multiplying it with renormalization constant Z_G. The renormalization transformation then reads: $G_0^n = Z_G^{-\frac{n}{2}} G^n$. This transformation of n-point function should be balanced with the accompanying renormalization

transformations of its parameters, so that the physical observables will stay independent of the scale. To see how G^n behaves under the shifts of its parameters when the renormalization scale is changed, we study the differential equation:

$$\mu\frac{\mathrm{d}}{\mathrm{d}\mu}G_0^n = \mu\frac{\mathrm{d}}{\mathrm{d}\mu}Z_G^{-\frac{n}{2}}G^n = 0 \tag{1.25}$$

$$\Rightarrow \left[\mu\frac{\partial}{\partial\mu} + \beta(g)\frac{\partial}{\partial g} + n\gamma + \gamma_m m\frac{\partial}{\partial m}\right]G^n = 0\,, \tag{1.26}$$

where we have defined the dimensionless functions:

$$\beta(g) = \mu\frac{\partial}{\partial\mu}g\,, \quad \gamma = \frac{1}{2}\mu\frac{\partial}{\partial\mu}\ln Z_G\,, \quad \gamma_m = -\mu\frac{\partial}{\partial\mu}\ln Z_m\,, \tag{1.27}$$

where Z_m is the mass renormalization constant. The β-function $\beta(g)$ describes the running of the gauge coupling with respect to the energy scale μ. Similarly, the mass anomalous dimension γ_m gives the running of the mass. Eq. (1.26) is known as the Callan-Symanzik equation [18, 19].

The zeroes of the β-function give the fixed points of the theory. The fixed points can be divided into two classes depending on the slope of the β-function at that point. If the slope is negative $\partial_g\beta(g) < 0$ we have a stable ultraviolet (UV) fixed point and if the slope is positive $\partial_g\beta(g) > 0$ we have an infrared (IR) stable fixed point. The location of said fixed points depend on the scheme, but the existence is scale invariant. This is clear when we look at a scheme transformation $G(g) = g'$. Now if $\beta(g) = 0$ it follows:

$$\beta'(g') = \frac{\partial G}{\partial g}\beta(g) = 0\,. \tag{1.28}$$

Furthermore, since the type of the fixed point (UV or IR) is a physical quantity, the derivative of the β-function at fixed point $\partial_g\beta(g)|_{\beta(g)=0}$ is scheme invariant [20]:

$$\frac{\partial\beta'(g')}{\partial g'} = \frac{\partial}{\partial g'}\left[\frac{\partial G}{\partial g}\beta(g)\right] = \left[\frac{\partial}{\partial g'}\left(\frac{\partial G}{\partial g}\right)\right]\beta(g) + \left(\frac{\partial G}{\partial g}\right)\left(\frac{\partial g}{\partial g'}\right)\frac{\partial\beta(g)}{\partial g} = \frac{\partial\beta(g)}{\partial g}\,. \tag{1.29}$$

The mass anomalous dimension γ_m is also a scheme invariant at fixed points. In Eq. (1.27) γ_m was defined with respect to mass renormalization constant Z_m, which transforms with a multiplicative function F_m under scheme transformations: $Z_m(g)F_m(G) = Z'_m(g')$. Similarly to Eq. (1.28) we can see [20]:

$$\begin{aligned}\gamma'_m(g') &= -\mu\frac{\partial}{\partial\mu}\ln\left(F_m(g)Z_m(g)\right) = \gamma_m(g) + \mu\frac{\partial}{\partial g}\frac{\partial g}{\partial\mu}\ln F_m \\ &= \gamma_m(g) + \left(\frac{\partial}{\partial g}\ln F_m\right)\beta(g)\,,\end{aligned} \tag{1.30}$$

and since $\beta(g) = 0$, we have shown the scheme invariance of γ_m.

The β-function and γ_m can be calculated in perturbation theory. The full perturbative expansions are scheme dependent, but the first two terms of the β-function, $\beta(g) = -2\beta_0 g^3 - 2\beta_1 g^5 + \cdots$, can be shown to be scheme independent by writing an expansion for a scheme transformation around $g = 0$: $g' = G(g) = g + G_1 g^3 + \mathcal{O}(g^5)$. There is no G_0 coefficient as the tree level coupling is unambiguous. Now the first two terms in the perturbative β-function read [20–23]:

$$\begin{aligned}\beta'(g') &= \left[1 + 3G_1 g^2 + \mathcal{O}(g^4)\right]\left[-2\beta_0 g^3 - 2\beta_1 g^5 + \mathcal{O}(g^7)\right] \\ &= -2\beta_0\left[(g')^3 - 3G_1(g')^5\right] - \left[2\beta_1 + 6\beta_0 G_1\right](g')^5 + \mathcal{O}(g^7) \\ &= -2\beta_0(g')^3 - 2\beta_1(g')^5 + \mathcal{O}(g^7)\,, \end{aligned} \tag{1.31}$$

which shows the invariance. Likewise, since $\beta = \mathcal{O}(g^3)$, it can be seen directly from Eq. (1.30) that γ_m is invariant up to the first order of the perturbative expansion.

For massless non-Abelian gauge theories, such as QCD, the β-function has been calculated up to the 5-loop level [24–28] in the $\overline{\text{MS}}$ scheme [29]. The scheme invariant part is:

$$\beta(g) = -\frac{\beta_0}{16\pi^2} g^3 - \frac{\beta_1}{(16\pi^2)^3} g^5 + \mathcal{O}(g^7) \tag{1.32}$$

$$\beta_0 = \frac{11}{3} C_2(A) - \frac{4}{3} T(R) N_f \tag{1.33}$$

$$\beta_1 = \frac{34}{3} C_2^2(A) - \frac{20}{3} C_2(A) T(R) N_f - 4 C_2(R) T(R) N_f\,, \tag{1.34}$$

where the quadratic Casimir operator $C_2(R)$ and the group generator $T(R)$ are evaluated either at generic gauge group representation R or adjoint representation A. Meanwhile, γ_m is known up to 5-loop level [30–33] in the $\overline{\text{MS}}$ scheme. The scheme invariant part is:

$$\gamma_m(g) = -\frac{\gamma_0}{16\pi^2} g^2 + \mathcal{O}(g^4)\,, \text{where} \quad \gamma_0 = 6C_2(R)\,. \tag{1.35}$$

1.5 Conformal window

The behavior and the fixed point structure of the β-function (1.32) depends on the number of fermions in the theory N_f. For small number of fermions i.e. QCD with $N_f = 6$, both terms in the two loop expansion are negative, i.e. $\beta_{0,1} > 0$, and the coupling will approach zero at high energy scales, which causes the quarks and gluons to behave like free particles at high energies. On the other hand, the coupling will grow rapidly at low energies, which makes quarks and gluons confine into hadrons. These two qualities follow from the asymptotic freedom of the

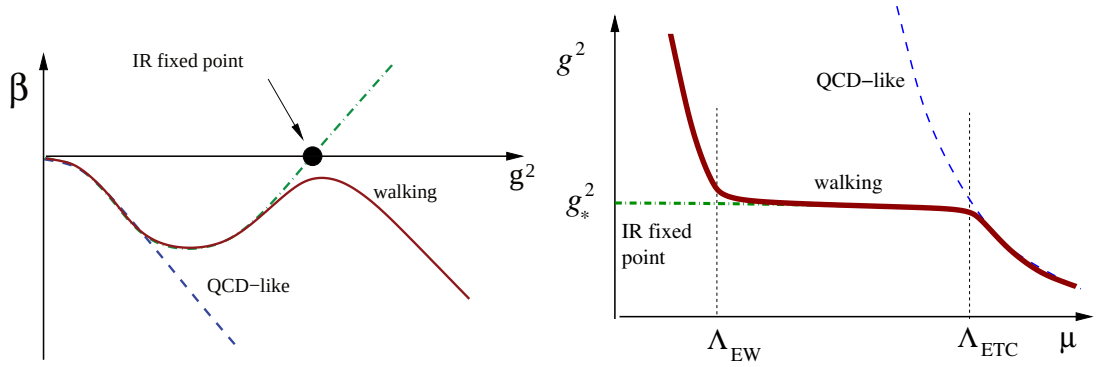

Figure 1.2: Schematic explanation of the different behaviors of the β-function and coupling for non-Abelian gauge theories: QCD-like, walking, and IRFP.

theory. These theories are expected to have chiral symmetry breaking similarly to QCD.

As the number of fermions is increased, the coefficient β_1 becomes negative:

$$N_f > N_f^{\text{crit}} = \frac{17C_2^2(A)}{10C_2(A)T(R) - 6C_2(R)T(R)} \tag{1.36}$$

and the β-function, instead of running to negative infinity, will start to grow at large couplings towards a nontrivial infrared fixed point (IRFP). At the IRFP the theory will become conformal and the chiral symmetry breaking is lost. The conformal theories are scale invariant and all masses and correlation functions will run to zero with universal power law [34, 35]:

$$M \propto m_q^{\frac{1}{1+\gamma_m}}\,, \tag{1.37}$$

where the exponent is mandated by the mass anomalous dimension γ_m and m_q is the quark mass. In fact, at the IRFP, the mass is the only relevant direction of the renormalization group flow and the gauge coupling becomes irrelevant. In the vicinity of the IRFP, the β-function will have a linear behavior and the slope in which the β-function approaches the IRFP is given by the leading irrelevant exponent of the coupling $\gamma_g = \partial_g \beta$.

When the number of fermions is set to N_f^{crit}, the coupling at the IRFP tends to be large. Since the perturbation theory relies on the couplings to be small, the exact lowest number of fermions at which the theory becomes conformal is unknown and non-perturbative methods are required. However, when the number of fermions is increased, the IRFP coupling decreases until at some point it becomes perturbatively reliable. This perturbatively stable IRFP is called the Banks-Zaks fixed point [36].

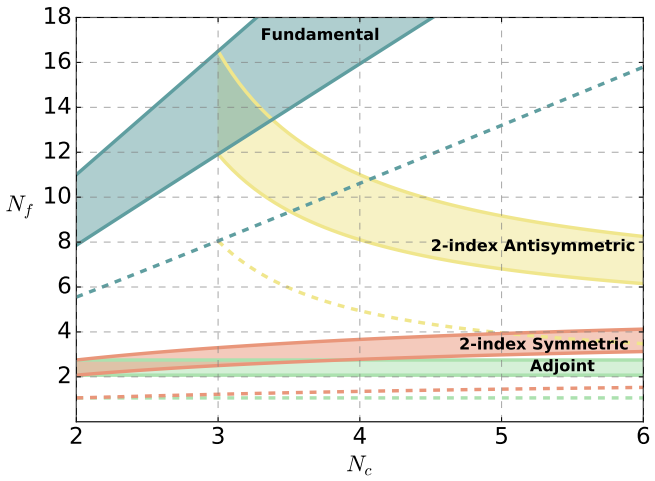

Figure 1.3: Conformal window for different fermion representations and various number of colors N_c. The upper solid line is the perturbative loss of asymptotic freedom. The lower solid line is the ladder approximation result, and the lower shaded band is the perturbative estimate from Eq. (1.36) [40].

When the number of flavors is increased past the Banks-Zaks fixed point, at some point the IRFP will merge with the Gaussian fixed point at $g = 0$ and β_0 will become negative. This happens at $N_f > N_f^{\max} = 11C_2(A)/4T(R)$. With N_f greater than $N_f^{\max}$, the theory loses both asymptotic freedom and conformality.

The range $N_f^{\text{crit}} < N_f < N_f^{\max}$, in which the theory is conformal, is called the conformal window. The upper limit of the conformal window is known from perturbation theory, meanwhile the lower boundary has to be found via non-perturbative lattice simulations or be approximated analytically. These approximations include: the methods [37–40] that use the ladder-like approximations of the Swinger-Dyson functions to find the lowest N_f breaking the chiral symmetry, the ACS conjecture [41] that has slightly different argument for the chiral symmetry breaking, the methods [42–44] that use the all-orders-beta-function motivated by the supersymmetry, and the metric confinement criterion [45] that uses the properties of transverse gluon propagators. In figure 1.3 we present the estimate of the conformal window for different group representations and various number of colors using the ladder approximation and Eq. (1.36) [40].

Right below the conformal window, there might exist a region in which the theory first approaches the IRFP but then runs to zero and is chirally broken. A theory with property like that would have a energy region in which the coupling runs slow and stays nearly constant. Slow running of the coupling is called walking. As the masses run to zero at the IRFP, the easiest way of creating a walking

theory is to add explicit masses, which will break the conformal invariance.

1.6 Beyond the Standard Model

The Standard Model with minor extensions, such as the neutrino masses, explain all the concurrent experimental results in the particle physics. However, this does not mean that the particle physics is a complete theory, because many theoretical questions still remain unanswered. The Higgs particle itself is particularly problematic being the only fundamental scalar in the Standard Model. The Higgs sector has to be fine tuned, since there is no natural scale separation between the electroweak scale and the Planck scale. This is known as the hierarchy problem. Other problems of the Standard Model are related to the matter-antimatter asymmetry, dark matter and dark energy, and the fact that there is no known quantum theory for the gravity.

In this thesis, we focus on the vacuum phase structure of gauge models with multiple fermions and are especially interested on models that could exhibit a walking behavior. Naturally, these models cannot answer every problem within the known theoretical particle physics, but they could offer a way forward in some of the problems, mainly the Higgs hierarchy problem. Of practical theoretical suggestions, this walking behavior has been utilized in: unparticle models [46, 47], and composite Higgs scenarios. For the purposes of this thesis, we use a particular type of composite Higgs model called technicolor [48–51] as a motivational example.

The basic idea behind composite Higgs models is to replace the fundamental scalar Higgs with a composite particle. If this particle is due to a strongly interacting theory, akin to QCD, the electroweak symmetry breaking would then be replaced by the chiral symmetry breaking. The effect of the QCD chiral breaking on the electroweak breaking can be calculated and it turns out to be minuscule. With only the QCD chiral symmetry breaking the mass of the W boson would become $m_W = \frac{1}{2} g F_\pi \sim 29 MeV$, where F_π is the pion decay constant. With the QCD chiral symmetry breaking, the W boson mass would be too small, and therefore a new strongly interacting theory is needed. The simplest addition is a scaled version of QCD, possibly with different number of colors N_c or flavors N_f. This allows the tuning of the pion decay constant in such a way that the weak gauge bosons gain correct masses. These theories are known as technicolor theories [48, 49].

However, in order to explain all properties of the Higgs boson, we need not only the correct weak sector but also the correct Yukawa terms. As the Higgs particle is now made of fermions itself, the resulting Lagrangian will have four

fermion interaction operators. These models are called the extended technicolor models (ETC) [50, 51]. Naïvely, we can write the Lagrangian for the masses:

$$\mathcal{L}_{\mathrm{m}} = \alpha \bar{Q} u_R Q \bar{u}_R + \beta \bar{Q} u_R T \bar{t}_R + \gamma \bar{T} t_R T \bar{t}_R \,, \tag{1.38}$$

where Q and u are the Standard Model particles (1.2), T and t are the new technicolor doublet and singlet respectively, and α, β, γ are constants. The first term in $\mathcal{L}_{\mathrm{m}}$ generates flavor changing neutral currents (FCNC), which are heavily bounded by the experimental results and so far have not been observed. This indicates that the parameter α must be small. However at the technicolor scale, the theory has no limits for the value of parameter α. On the other hand, the amount of FCNCs is small at the electroweak scale, so the bulk of the masses could be generated by the renormalization flow from the technicolor scale to the extended technicolor scale. The evolution of quark condensate is determined by the mass anomalous dimension (1.27):

$$\frac{\mathrm{d}}{\mathrm{d}\mu}\left(m\bar{Q}Q\right) = m\frac{\mathrm{d}\bar{Q}Q}{\mathrm{d}\mu} - \frac{m\gamma_m}{\mu}\bar{Q}Q = 0 \tag{1.39}$$

$$\Rightarrow\ (\bar{Q}Q)_{\mathrm{ETC}} = \exp\left[\int_{\Lambda_{\mathrm{TC}}}^{\Lambda_{\mathrm{ETC}}} \frac{\gamma(\mu)}{\mu}\mathrm{d}\mu\right](\bar{Q}Q)_{\mathrm{TC}}\,. \tag{1.40}$$

This implies that either γ_m has to be large around of order 1, or the coupling has to be walking so that the scale separation between Λ_{TC} and Λ_{ETC} is long enough for the integral to accumulate mass.

As the walking behavior is expected to occur near the lower edge of the conformal window, which tends to be at large gauge coupling, a non-perturbative analysis is called for to classify potential model candidates for beyond the standard model scenarios. In this thesis we perform non-perturbative lattice simulations and measure both the running of the coupling and the mass anomalous dimension.

CHAPTER 2

Lattice field theory

2.1 Monte Carlo simulations

The Feynman path integral [52] of the QCD partition function Z can be formulated as:

$$Z = \int \mathcal{D}A_\mu \mathcal{D}\bar{\psi}\mathcal{D}\psi \, e^{iS_{\mathrm{QCD}}(A_\mu,\bar{\psi},\psi)} \,, \tag{2.1}$$

which is written using the action $S_{\mathrm{QCD}} = \int dx^4 \, \mathcal{L}_{\mathrm{QCD}}$ (1.19). The imaginary exponent in the path integral causes the integral to fluctuate with high frequency, which complicates numerical integration and makes simulations costly. The Euclidean path integral formalism solves this problem by analytically continuing the domain of integration into imaginary time and changing the metric from Minkowski to Euclidean. In order to change the metric, we perform a Wick rotation that rotates the time coordinate counterclockwise transforming it into imaginary time $t \equiv x_0 \to ix_4 \equiv i\tau$. The path integral takes the form:

$$Z = \int \mathcal{D}A^{\mathrm{E}}_\mu \mathcal{D}\bar{\psi}^{\mathrm{E}}\mathcal{D}\psi^{\mathrm{E}} e^{\bar{\psi}^{\mathrm{E}}(i\not{\partial}-m)\psi^{\mathrm{E}} - \frac{1}{4}F^{\mathrm{E}}_{\mu\nu}F^{\mu\nu}_{\mathrm{E}}} \tag{2.2}$$

where we have written the Euclidean QCD action explicitly. The rest of this thesis is written in the Euclidean formulation and the superscript E is dropped from all the equations that follow.

The elements of fermion fields $\bar{\psi}$ and ψ are Grassmann numbers, which makes them cumbersome to implement in computer simulations. To ease the numerical calculations, we integrate the fermion fields out as a simple Gaussian integral. An arbitrary observable O now has an expectation value:

$$\langle O \rangle = \frac{1}{Z} \int \mathcal{D}A_\mu \, O \det(\not{D} + m) \, e^{-\frac{1}{4}\int d^4x \, F_{\mu\nu}F^{\mu\nu}} \,. \tag{2.3}$$

While the fermionic determinant makes the simulations more manageable, it is highly non-local and still expensive to compute numerically. Some remedies for the fermion determinant will be discussed in section 2.6.

The (2.3) can be integrated numerically in order to measure the expectation value on the lattice. However, the integral (2.3) has extremely high dimension, which renders naïve numerical integration methods unfeasible. The way forward is to note that just a small subset of link configurations U contribute significantly to the final result. So, instead of integrating over all possible link configurations we should stochastically sample a probability distribution P:

$$P = \frac{1}{Z} e^{-\frac{1}{4}\int d^4x\, F_{\mu\nu}F^{\mu\nu} + \ln\det(\not{D}_\mu + m)}\,. \tag{2.4}$$

After sampling the probability distribution N times, we find the expectation value as an average $\langle O\rangle = N^{-1}\sum_i O_i + \mathcal{O}(N^{-\frac{1}{2}})$. This method is known as importance sampling and is exact in the limit $N \to \infty$. However, truncating the sum into a finite number of trajectories, causes an error of order $\mathcal{O}(N^{-\frac{1}{2}})$ because of the central limit theorem [53].

Now, we must find way to generate configurations that are sampled with this probability distribution P. Multiple algorithms can generate such configurations and one example of such procedure is the Metropolis algorithm [54, 55]. The Metropolis algorithm starts with a initial gauge field configuration U_0, after which following steps are taken:

1. Generate a new U_{k+1} by doing a small random change to U_k.
2. Evaluate the difference: $\Delta S = S(U_{k+1}) - S(U_k)$.
3. If $\Delta S \leq 0$ accept the change.
4. If $\Delta S \geq 0$ accept with probability $e^{-\Delta S}$.

Since the gauge field configurations U_k must abide the gauge symmetry, the step 1 must be taken so that the Haar measure of the gauge group is not broken. The gauge configurations generated through these steps generate a Markov chain. In Markov chains, each state U_k is a random variable depending only on the previous step U_{k-1}, and hence every state within the Markov chain can be regarded as a U_0. However, this does not mean that the measured U_k are independent of each other. The algorithm will generate autocorrelations between the measurements which will have to be taken into account in the final error analysis.

This Markov chain property is an essential requirement for the simulation time average to approach the ensemble average as $N \to \infty$. Another requirement for the Metropolis algorithm to thermalize into a stable probability distribution is given by the detailed balance condition [56]. The detailed balance condition is satisfied when in a Markov chain, the probability of finding a system in the

state U and then have it to transition to the state U' equals to the probability of finding the system in the state U' and then transitioning to the state U: $P(U)P(U \to U') = P(U')P(U' \to U)$.

When fermions are included, the performance of the simulation can be improved further by using a hybrid Monte-Carlo algorithm [57] (HMC) instead of the Metropolis algorithm. The HMC algorithm extends the Metropolis algorithm by replacing the random change generating step 1 with a short molecular dynamics simulation followed by the Metropolis test described in steps 2–4. In the molecular dynamics simulation, we integrate the Hamiltonian:

$$H = \frac{1}{2}\mathrm{Tr}\,\Pi^2 + S = (\Pi^a)^2 + S\,, \tag{2.5}$$

where $\Pi = \Pi^a_{x,\mu}\lambda^a$ is the traceless and Hermitean gauge field momentum, that will be initialized a Gaussian distribution, and λ^a is the gauge group generator. Now the evolution of the gauge field is governed by the equations of motion

$$\partial_\tau \Pi = -\frac{\partial H}{\partial U}\,, \quad \text{and} \quad \partial_\tau U = i\Pi U\,, \tag{2.6}$$

where we have introduced a fictitious simulation time coordinate τ. The equations of motion are then numerically integrated with algorithms such as leapfrog or Omelyan integrators [58, 59]. The error of the chosen integrator directly affects the acceptance ratio in the Metropolis step. Furthermore, when the numerical integration algorithm is not exact, i.e $\Delta\tau \neq 0$, it has to satisfy two additional conditions in order to satisfy the detailed balance condition [60]: Firstly, the integration must be time reversible and secondly, the phase space volume must be conserved so that: $dU_k d\Pi_k = dU_{k+1} d\Pi_{k+1}$.

Overall, the HMC algorithm allows us to reach representative sampling with smaller amount of iterations than the simple Metropolis sampling. This is because the conservation of Hamiltonian (2.5) allows generation of configurations further apart from each other than simple small random change in Metropolis step 1.

2.2 Quantum fields on the lattice

The simplest way to discretize a four dimensional space-time is to create an isotropic hypercubic box of size $L^4 = (Na)^4$, where the each side of the box has N sites that are one lattice spacing a apart from each other. This discretizes the definition of a coordinates, so that every direction becomes $x_\mu \to n_\mu a$, where n_μ enumerates the L. The discretization also reduces the symmetry of the space-time from full Poincaré group of continuous rotations and translations into a discrete

symmetry, where only rotations by $\pi/2$ and translations by a are invariant. With a finite box, we also have to choose the boundary conditions. A common choice is to make the boundaries periodic by setting sites n_μ and $n_\mu + L$ equal. Alternatively, one can use fixed boundaries in one or more directions. A common choice is to have Dirichlet boundaries on the temporal directions $\psi(x_0 = 0) = \psi(x_0 = L) = 0$. In this thesis, we will use the periodic boundaries on spatial directions and Dirichlet boundaries on temporal directions. This choice is motivated by the Schrödinger functional method, and explained in detail in section 2.5.

The discretization of the space-time also discretizes the mathematical operators. The integrals are replaced by sums and derivatives with finite differences:

$$\psi(x) \to \psi(na) \tag{2.7}$$

$$\int d^4x \to a^4 \sum_n \tag{2.8}$$

$$\partial_\mu \psi \to \begin{cases} \frac{1}{a}\left(\psi_{x+a\hat{\mu}} - \psi_x\right) \\ \frac{1}{a}\left(\psi_x - \psi_{x-a\hat{\mu}}\right) \end{cases} = \frac{1}{2a}\left(\psi_{x+a\hat{\mu}} - \psi_{x-a\hat{\mu}}\right) \tag{2.9}$$

$$\Box\psi(x) \to \frac{1}{a^2}\sum_\mu \left(\psi(na + \hat{\mu}a) + \psi(na - \hat{\mu}a) - 2a\psi(na)\right) \tag{2.10}$$

$$\mathcal{D}\psi \to \prod_n d\psi(na) \tag{2.11}$$

$$p_\mu = \frac{2\pi}{L} n_\mu \,, \tag{2.12}$$

where $\hat{\mu}$ is the unit vector in x_μ direction and $\Box$ is the d'Alembert operator. In (2.9) we show that the forward and backward partial derivatives can be combined into a symmetrized derivative operator with smaller discretization errors. The momentum p_μ is discretized by the boundary conditions.

The process of discretizating the space time into a hypercubic lattice regularizes the theory naturally. This lattice regularization shares similarities with the cut-off regularization. By taking a Fourier transformation of the field ψ:

$$\tilde{\psi}(p) = a^4 \sum_x e^{ipx}\psi(x) \,, \tag{2.13}$$

we notice that the momentum space is periodic $p_\mu = p_\mu + 2\pi/a$ and the momentum is limited into the Brillouin zone $-\pi/a < p_\mu < \pi/a$.

In order to write the QCD action in the lattice formalism we need both the field strength part and the covariant derivative, both of which depend on the gauge field A_μ. However, satisfying the gauge invariance of Eq. (1.20) on a finite lattice turns out to be non-trivial. The finite differences in lattice derivatives depend on coordinates at two distinct points. On the other hand, gauge transformations are

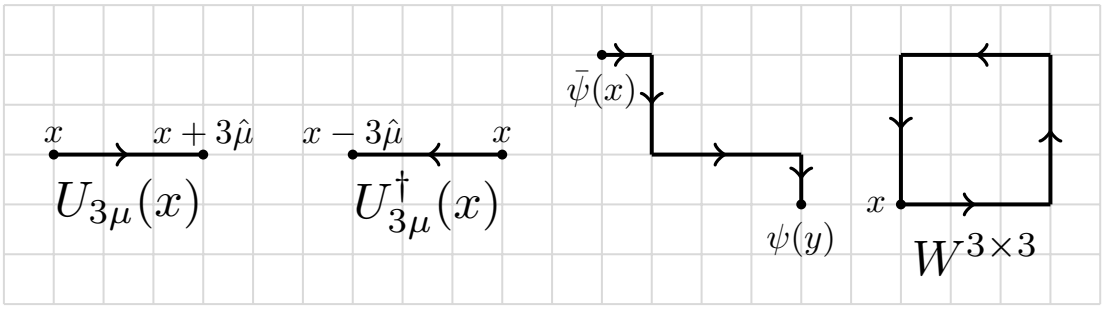

Figure 2.1: From left to right: gauge links U and $U^{\dagger}$ three times their usual size and gauge invariant objects: connected fermion fields, and example of Wilson loop.

local and defined separately on each point. This complicates the definition of gauge invariant finite differences. The solution is to associate the gauge fields to links between the lattice sites as a parallel transport from x to direction μ: $U_\mu(x)$. The gauge links $U_\mu(x)$ (illustrated in figure 2.1) form a group by abiding to the group rules: the zero-length parallel transport from point to itself is identity function, the path can be decomposed to sub-paths $U_{2\mu}(x) = U_\mu(x)U_\mu(x+\hat{\mu})$, and the inverse matrix $U_\mu^{-1} = U_\mu^\dagger$ traverses the link to opposite direction. The gauge link should also satisfy the gauge invariance by transforming as: $U_\mu(x) \to V(x)U_\mu(x)V^\dagger(x+\hat{\mu})$. In order to find a parallel transport for a arbitrary path s, we can solve a differential equation:

$$\frac{d}{ds}U(s) = \frac{dx_\mu}{ds} igA_\mu U(s) \tag{2.14}$$

$$\Rightarrow U(s) = Pe^{ig\int_s ds \frac{dx_\mu}{ds} A_\mu}\,, \tag{2.15}$$

where P stands for path ordering, which makes sure all the non-Abelian fields are multiplied in correct order. A single gauge link between two lattice sites can be approximated more clearly as:

$$U_\mu(x) = e^{igaA_\mu\left(x+\frac{1}{2}\hat{\mu}a\right)}\,. \tag{2.16}$$

This allows us to define two kinds of gauge invariant paths. First is a path connecting fermion field to an anti-fermion field. For example:

$$\bar{\psi}(x)U_\mu(x)U_\nu(x+\hat{\mu})\cdots U_\mu(y-\hat{\nu})\psi(y)\,. \tag{2.17}$$

The second is closed loop also known as Wilson loop when the loop is closed within the lattice and Polyakov loop when the loop is a straight line connected through the periodic boundary conditions. The simplest Wilson loop is a plaquette:

$$W^{1\times 1}_{\mu\nu} = \mathrm{Re}\,\mathrm{Tr}\left(U_\mu(x)U_\nu(x+\hat{\mu})U^\dagger_\mu(x+\hat{\nu})U^\dagger_\nu(x)\right)\,. \tag{2.18}$$

Both of these gauge invariant objects are presented in figure 2.1.

We can now write $\mathcal{O}(a^2)$ version of the lattice covariant derivative by including gauge fields into Eq. (2.9). The Wilson Dirac operator now reads:

$$D_\mu = \frac{1}{2}\left(D^f_\mu + D^b_\mu\right)\psi(x) \tag{2.19}$$

$$D^f_\mu = \frac{1}{a}\left[U_\mu(x)\psi(x+a\hat{\mu}) - \psi(x)\right] \tag{2.20}$$

$$D^b_\mu = \frac{1}{a}\left[\psi(x) - U^\dagger_\mu(x-a\hat{\mu})\psi(x-a\hat{\mu})\right] . \tag{2.21}$$

This allows us finally write the fermionic part of the QCD action as:

$$S^{\text{naive}}_{\text{fermion}} = a^4 \sum_x \left[\bar{\psi}(x)(\gamma^\mu D_\mu + m)\psi(x)\right] . \tag{2.22}$$

As we shall see in the next section, this is a naïve way to formulate the QCD action, and will lead to problems.

For the gauge part of the action, the gauge invariant Wilson loop (2.18) turns out to be useful. By using the Campbell-Baker-Hausdorff formula:

$$e^{gA}e^{gB} = e^{g(A+B)+\frac{g^2}{2}[A,B]+\mathcal{O}(g^3)} , \tag{2.23}$$

where A and B are general non-Abelian matrices, we can use Eq (2.16) and write the $W^{1\times1}$ plaquette in an open form:

$$\begin{aligned} W^{1\times1} &= e^{-igaA_\mu(x)}e^{-igaA_\nu(x+\hat{\mu})}e^{-igaA_\mu(x+\hat{\nu})}e^{-igaA_\nu(x)} \\ &= e^{-igaA_\mu(x)-igaA_\nu(x+\hat{\mu})-iga^2\partial_\mu A_\nu(x)-\frac{g^2a^2}{2}[A_\mu,A_\nu]} \\ &\quad e^{igaA_\mu(x)+igaA_\nu(x+\hat{\mu})+iga^2\partial_\nu A_\mu(x)-\frac{g^2a^2}{2}[A_\mu,A_\nu]} \\ &= e^{iga^2(\partial_\nu A_\mu-\partial_\mu A_\nu+ig[A_\mu,A_\nu])+\mathcal{O}(a^3)} \\ &= e^{iga^2F_{\mu\nu}(x)+\mathcal{O}(a^3)} . \end{aligned} \tag{2.24}$$

Furthermore, we expand the result as a Taylor series:

$$W^{1\times1} \approx 1 + iga^2F_{\mu\nu} - a^4\frac{g^2}{2}F_{\mu\nu}F^{\mu\nu} + \mathcal{O}(a^6) , \tag{2.25}$$

and observe the possibility to write the Yang-Mills gauge action using the plaquette. The result is known as the Wilson gauge action [61]:

$$S_{\text{G}} = \beta_L \sum_x \sum_{\mu<\nu}\left(1 - \frac{1}{N_c}\text{Re}\,\text{Tr}\; W^{1\times1}\right) , \tag{2.26}$$

where $\beta_L = 2N_c/g^2$. In the continuum, when $a \to 0$ and $L \to \infty$, this reproduces the traditional Yang-Mills action up to $\mathcal{O}(a^2)$ accuracy. Actions with reduced lattice artifacts are discussed more in the section 2.4.

2.3 Fermions on the lattice

As stated in the previous section, the naïve fermion action (2.22) has some problems. In order to manifest these problems, we inspect the correlation function $\langle\psi\bar{\psi}\rangle$. This expectation value can be solved as a simple Gaussian integral by using Eq. (2.3) [53]:

$$\langle\psi_\alpha(x)\bar{\psi}_\beta(y)\rangle = K^{-1}_{\alpha\beta}(x,y)\,, \tag{2.27}$$

where

$$K_{\alpha\beta}(x,y) = \frac{1}{2}\left(\gamma_\mu\right)_{\alpha\beta}\left[\delta_{y,x+\hat{\mu}} - \delta_{y,x-\hat{\mu}}\right] + m\delta_{x,y} \tag{2.28}$$

and

$$\sum_{\lambda,y} K^{-1}_{\alpha\lambda}(x,y)K_{\lambda\beta}(y,z) = \delta_{x,z}\delta_{\alpha,\beta}\,, \tag{2.29}$$

which is solved by taking the Fourier transform:

$$\langle\psi(x)_\alpha\bar{\psi}_\beta(y)\rangle = \lim_{a\to 0}\int_{-\frac{\pi}{a}}^{\frac{\pi}{a}} \frac{d^4p}{(2\pi)^4}\,\frac{\left[-\gamma^\mu\tilde{p}_\mu + m\right]_{\alpha\beta}}{\sum_\mu \tilde{p}_\mu^2 + m^2}e^{ip(x-y)}\,, \tag{2.30}$$

where the lattice momentum $\tilde{p}_\mu$ reads:

$$\tilde{p}_\mu = \frac{1}{a}\sin(ap_\mu)\,. \tag{2.31}$$

Around zero the lattice momentum corresponds to continuum momentum with relation $\tilde{p}_\mu \sim p_\mu$, but around the large momentum of $p_\mu \sim 1/a$, the lattice momentum deviates from the continuum momentum towards zeroes at the edges of Brillouin zone. These zeros effectively give rise to fermionic particles of their own. As a result, every dimension of space-time doubles the fermions. Therefore the naïve fermion action (2.22) in four dimensions has $2^d = 16$ fermions instead of one.

To tackle this problem Wilson introduced an order $\mathcal{O}(a)$ correction term that removes the doubling, vanishes in the continuum limit, and does not affect physical measurements [61].

$$S^{\text{Wilson}}_{\text{fermion}} = S^{\text{naive}}_{\text{fermion}} - \frac{r}{2}\sum_x \bar{\psi}(x)\Box\psi(x)\,, \tag{2.32}$$

where $\Box$ is the d'Alembert operator (2.10) and r is the Wilson parameter. Now, the fermion action in the lattice formulation can be rewritten as:

$$\begin{aligned}
S_{\text{fermion}} &= \bar{\psi}(\not{D} + m)\psi \\
&= \frac{am + r}{a}\bar{\psi}\psi + \frac{1}{2a}\bar{\psi}\left[(\gamma^\mu - r)U_\mu(x)\psi(x+\hat{\mu}) - (\gamma^\mu - r)U^\dagger_\mu(x-\hat{\mu})\psi(x-\hat{\mu})\right] \\
&= \bar{\psi}^{\text{L}}(x)\left[\delta_{x,y} - \kappa\left\{(r-\gamma^\mu)U_\mu(x)\delta_{x,y-\hat{\mu}} + (r+\gamma^\mu)U^\dagger_\mu(x-\hat{\mu})\delta_{x,y+\hat{\mu}}\right\}\right]\psi^{\text{L}}(y) \\
&= \bar{\psi}^{\text{L}}M^{\text{W}}\psi^{\text{L}}\,,
\end{aligned} \tag{2.33}$$

where we have introduced a hopping parameter $\kappa^{-1} = 2am + 8r$, which encodes the fermion coupling between different lattice points, and rescaled the fermion fields as $\psi^{\mathrm{L}} = \psi/\sqrt{2\kappa}$. We call the operator M^{W} the Wilson-Dirac operator.

With Wilson fermion action, Eq. (2.27) will give lattice momenta akin to Eq. (2.31), but the scalar part of the Dirac operator m now has a momentum dependence:

$$\tilde{m}(p) = m + 2\frac{r}{a}\sum_{p}\sin^2(\frac{1}{2}ap_\mu)\,. \tag{2.34}$$

Because this term now diverges at the edges of the Brillouin zone when $a \to 0$, we have effectively removed the spurious particle poles that caused the fermion doubling. On the other hand, the momentum dependence of the scalar part of the Dirac operator breaks the chiral symmetry at vanishing mass, since the Wilson-Dirac operator M^{W} (2.33) no longer anticommutes with γ^5 when $m = 0$. In order to reach the zero mass with Wilson fermions, the hopping parameter κ must be tuned so that the mass vanishes.

Apart from Wilson fermions, other fermion formulations have been developed. Some commonly used formulations include, but are not limited to, staggered fermions [62, 63], domain wall fermions [64], and overlap fermions [65]. All the different fermion formulations solve some problems with lattice fermions, but none of them solve all the problems. A perfect lattice fermion action turns out to be impossible, because of the Nielsen-Ninomiya no-go theorem [66], which states that the lattice Dirac operator cannot satisfy all the following properties at once:

1. Translation invariance: D_μ is $2\pi/a$-periodic in momentum space
2. Locality: D_μ is continuous in momentum space
3. No fermion doubling: D_μ is invertible for $p \neq 0$
4. Chiral symmetry: $\gamma^5 D_\mu + D_\mu \gamma^5 = 0$
5. $D_\mu(p) \to i\gamma^\mu p_\mu$ when $a \to 0$ and p_μ is small

Our choice of discretization is to use Wilson clover fermions, which are introduced in the next section 2.4.

2.4 Improved actions

In the previous section we derived the Wilson fermion action (2.32) to the level where the leading order lattice discretization errors were linear in lattice spacing $\mathcal{O}(a)$. While all the lattice effects vanish in the continuum limit $a \to 0$, in

practice all the computer simulations are done with finite a. In order to accurately extrapolate the $a \to 0$ limit, one would need a collection of data generated at small lattice spacings and large lattice sizes. However, both the smaller lattice spacings and larger lattices tend to be slower and more expensive to simulate, which limits the accessible lattice spacings a.

In order to find actions with smaller discretization effect, a Symanzik improvement program [67–69] was proposed. In the Symanzik approach, the lattice cutoff effects are incorporated into an effective field theory in continuum. This is done by adding extra terms to the action, so that after the traditional dimension four operators, we have higher dimensional operators encoding the lattice effects at level $d-4$, for example: the dimension five operators will correspond to the errors linear in lattice spacing and the dimension six operators make up the quadratic errors. The effective field theory then has the action:

$$S_{\text{eff}} = \int d^4x \left(\mathcal{L}_0 + a\mathcal{L}_1 + a^2\mathcal{L}_2 + \cdots \right) , \tag{2.35}$$

where $\mathcal{L}_0$ is the original continuum Lagrangian, $\mathcal{L}_1$ has the dimension five terms, and so on.

For the effective field theory to correctly encode the underlying lattice field theory, it has to satisfy its symmetries, such as: the discrete lattice symmetries, the flavor rotation symmetry $SU(N_f)$, and the gauge symmetry. These symmetry constraints greatly limit the number of allowed operators. For example, the Wilson fermion action (2.32) only has five independent dimension five operators at the level of linear discretization errors [70]:

$$\begin{aligned}
&\mathcal{O}_1 = \bar{\psi} i\sigma_{\mu\nu} F^{\mu\nu} \psi \,, && \mathcal{O}_2 = \bar{\psi} D^f_\mu D^\mu_f \psi + \bar{\psi} D^b_\mu D^\mu_b \psi \,, \\
&\mathcal{O}_3 = m\text{Tr } F_{\mu\nu} F^{\mu\nu} \,, && \mathcal{O}_4 = m^2 \bar{\psi}\psi \,, \\
&\mathcal{O}_5 = m \left(\bar{\psi} \not{D}^f \psi + \bar{\psi} \not{D}^b \psi \right) .
\end{aligned} \tag{2.36}$$

By some mathematical trickery, one can absorb most of these operators into modifications of bare mass and coupling in $\mathcal{L}_0$. This leaves us with only the term $\mathcal{O}_1$ as long as we limit ourselves to what is called the on-shell improvement [71]. The improvement $\mathcal{O}_1$ is known as the clover term and its coefficient was calculated first by Sheikholeslami and Wohlert in [72]. The name clover comes from the four leafed clover shape of the lattice links when the field strength tensor $F_{\mu\nu}$ is

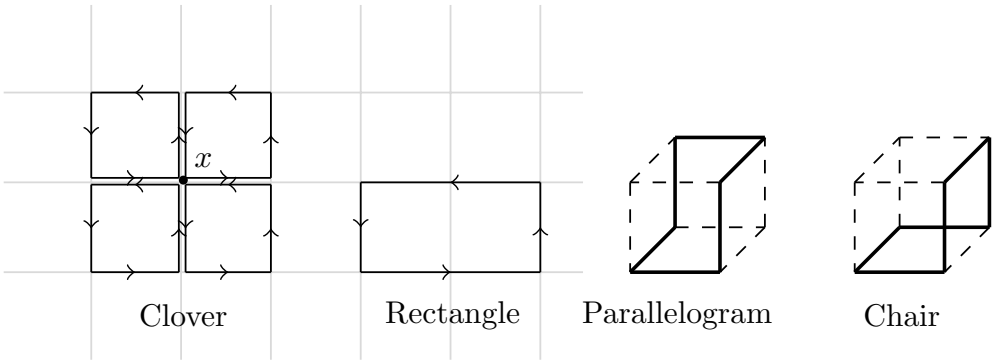

Figure 2.2: The dimension five operator: Clover, and dimension six operators: rectangle, parallelogram, and chair.

formulated on the lattice by using the Wilson loops (2.25):

$$F_{\mu\nu}(x) = \frac{1}{8a^2}\left(Q_{\mu\nu}(x) - Q_{\nu\mu}(x)\right) \tag{2.37}$$

$$\begin{aligned} Q_{\mu\nu} = {} & U_\mu(x)U_\nu(x+\hat{\mu})U_\mu^\dagger(x+\hat{\nu})U_\nu^\dagger(x) \\ & + U_\nu(x)U_\mu^\dagger(x+\hat{\nu}-\hat{\mu})U_\nu(x-\hat{\mu})U_\mu^\dagger(x-\hat{\mu}) \\ & + U_\mu^\dagger(x-\hat{\mu})U_\nu^\dagger(x-\hat{\mu}-\hat{\nu})U_\mu(x-\hat{\mu}-\hat{\nu})U_\nu(x-\hat{\nu}) \\ & + U_\nu^\dagger(x-\hat{\nu})U_\mu(x-\hat{\nu})U_\nu(x-\hat{\nu}+\hat{\mu})U_\mu^\dagger(x)\,. \end{aligned} \tag{2.38}$$

The clover term allows us to write the clover improved Wilson action in the lattice normalization (2.33):

$$S_{\text{clover}} = S_{\text{fermion}}^{\text{Wilson}} + a^5 i\kappa c_{\text{sw}} \sum_x \bar{\psi}^{\text{L}}(x) \sum_{\mu<\nu} \sigma_{\mu\nu} F^{\mu\nu} \psi^{\text{L}}(x) = \bar{\psi}^{\text{L}}(x) M_{x,y}^{\text{clover}} \psi^{\text{L}}(y)\,, \tag{2.39}$$

where $M_{x,y}^{\text{clover}}$ is given by:

$$(1 + \kappa c_{\text{sw}} \sum_{\mu<\nu} \sigma_{\mu\nu} F^{\mu\nu})\delta_{x,y} - \kappa \left\{ (r - \gamma^\mu) U_\mu(x) \delta_{x,y-\hat{\mu}} + (r + \gamma^\mu) U_\mu^\dagger(x-\hat{\mu}) \delta_{x,y+\hat{\mu}} \right\}\,, \tag{2.40}$$

and c_{sw} is the Sheikholeslami-Wohlert parameter, which has to be calculated for the theory one plans to simulate. This calculation can be done non-perturbatively using simulations [73] or perturbatively [74]. For the purposes of this thesis, we will use the tree level result: $c_{\text{sw}} = 1$, which has become the standard choice for smeared actions [75–77].

Analogously to the fermion action improvement, the Wilson gauge action be also improved with the Symanzik program. Since the Wilson gauge action is already quadratic in the lattice spacing, the improvement starts with the dimension six operators. Because of the symmetry constraints, there are only

three independent operators:

$$\mathcal{O}_1 = \mathrm{Tr}\ (D_\mu F^{\mu\nu} D_\mu F^{\mu\nu})\ ,\ \mathcal{O}_2 = \mathrm{Tr}\ (D_\mu F^{\nu\rho} D_\mu F^{\nu\rho})\ ,\ \mathcal{O}_3 = \mathrm{Tr}\ (D_\mu F^{\mu\rho} D_\nu F^{\nu\rho})\ , \tag{2.41}$$

where we sum over all the indices. All these operators are constructed with six gauge links as shown in figure 2.2.

The improved gauge action has a generic form:

$$S_{\mathrm{LW}} = \beta_L \sum_{i=0}^{3} c_i \mathrm{ReTr}\ (1 - P_i)\ , \tag{2.42}$$

where P_i is a loop of shape corresponding to operator $\mathcal{O}_i$, so that P_0 is the plaquette. The constants c_i can be chosen freely, as long as they satisfy the constraint $c_0 + 8c_1 + 16c_2 + 8c_2 = 1$ [78]. The two most commonly used choices for c_i include: the Lüscher-Weisz action [71] with $c_0 = 5/3$, $c_1 = -1/12$, and $c_{i>1} = 0$, and the Iwasaki action [79] with $c_0 = 3.648$, $c_1 = -0.331$, and $c_{i>1} = 0$. For the purposes of this thesis, we will use the Lüscher-Weisz action.

2.5 Schrödinger functional boundary conditions

Choosing the lattice boundaries correctly can simplify some parts of lattice calculations. In the Schrödinger functional method [80], we set the spatial directions to be periodic and impose fixed boundary conditions on the temporal boundaries. While there is some benefit in choosing the temporal boundaries to be proportional to external potentials, for the purposes of this thesis we choose the simplest constant Dirichlet boundaries defined on the lattice as:

$$\begin{aligned} &U_k(0,\mathbf{x}) = U_k(L,\mathbf{x}) = 1\,, && \psi(0,\mathbf{x}) = \psi(L,\mathbf{x}) = 0\,, \\ &U_\mu(x_0,\mathbf{x}) = U_\mu(x_0,\mathbf{x} + L\hat{\mathbf{k}})\,, && \psi(x_0,\mathbf{x}) = \psi(x_0,\mathbf{x} + L\hat{\mathbf{k}})\,, \end{aligned} \tag{2.43}$$

where k denotes coordinate in the spatial direction. These boundaries differentiate the time coordinate from the space coordinates and break time translation symmetry.

To take the disparity between temporal and spatial boundaries into account, the Wilson gauge action (2.26) has to be modified:

$$S_{\mathrm{G}} = \beta_L \sum_p \omega(p)\,(1 - U(p))\ , \tag{2.44}$$

where U is the trace of the plaquettes p. The term $\omega(p)$ weights the plaquettes depending on their position, and at tree level $\omega(p)$ is 1 everywhere expect on $x_0 = 0, L$, where $\omega(p) = \frac{1}{2}$. However, the fixed boundaries introduce new order

$\mathcal{O}(a)$ errors that can be counterbalanced by modifying $\omega(p)$ [70, 80–84]. In the first order of perturbation theory the weight of spatial plaquettes on the temporal boundaries become: $\omega(p) = \frac{1}{2}c_s(g_0^2)$, and the weight of time-like plaquettes attached to boundary become: $\omega(p) = c_t(g_0^2)$. For now, we set these perturbative constant to their tree level values $c_t = c_s = 1$. In similar fashion, the fermion action also gains weights with perturbative improvements c_s' and c_t' [85]. We also set these to unity.

Using the Schrödinger functional boundary conditions we can measure the pseudoscalar current f_P, the axial current f_A, and the boundary-to-boundary current f_1 as [81]:

$$f_A(x_0) = -a^6 \sum_{\mathbf{y},\mathbf{z}} \langle \bar{\psi}(x)\gamma_\mu\gamma_5\lambda^a\psi(x)\,\bar{\zeta}(\mathbf{y})\gamma_5\lambda^a\zeta(\mathbf{z})\rangle \tag{2.45}$$

$$f_P(x_0) = -a^6 \sum_{\mathbf{y},\mathbf{z}} \langle \bar{\psi}(x)\gamma_5\lambda^a\psi(x)\,\bar{\zeta}(\mathbf{y})\gamma_5\lambda^a\zeta(\mathbf{z})\rangle \tag{2.46}$$

$$f_1 = \frac{-a^{12}}{2L^6} \sum_{\mathbf{u},\mathbf{v},\mathbf{y},\mathbf{z}} \langle \bar{\zeta}'(\mathbf{u})\gamma_5\lambda^a\zeta'(\mathbf{v})\bar{\zeta}(\mathbf{y})\gamma_5\lambda^a\zeta(\mathbf{z})\rangle\,, \tag{2.47}$$

where ζ and ζ' are temporal source quark fields at $x_0 = 0$ and $x_0 = L$ respectively.These allow the convenient definition of the renormalization constant Z_P [86–88]:

$$Z_P = \frac{\sqrt{N_c f_1}}{f_p(\frac{L}{2})}\,. \tag{2.48}$$

Z_P will turn useful later in the section 3.7, where we use it to define the mass anomalous dimension γ_m (1.27).

As discussed in the section 2.3, the Wilson fermions (2.32) break chiral symmetry explicitly and require additive renormalization of the quark mass. With Schrödinger functional boundary conditions, we can measure the renormalized quark mass using the currents (2.45) and (2.46), with the tree-level PCAC relation [81]:

$$M(x_0) = \frac{1}{4}\frac{(\partial_0^b + \partial_0^f) f_A(x_0)}{f_P(x_0)}\,, \tag{2.49}$$

where ∂^f and ∂^b are the forward and backward lattice derivatives respectively.

2.6 Pseudofermions

In section 2.1, we noted that the determinant of the operator $M = (\not{D} + m)$ in Eq. (2.3) is a non-local term that is expensive to calculate. One solution is to ignore the determinant by setting it to unity. This quenched approximation

ignores the effects caused by sea quarks and makes the simulations effectively pure gauge by neglecting the fermion loops in the Feynman diagrams.

The fermion determinant in Eq. (2.3) is expensive to evaluate directly. More economically, fermions can be simulated using pseudofermions. In the pseudofermion method, we notice that instead of the determinant being a result of Grassmannian Gaussian integral, it could as well be a result of a Gaussian integral over complex pseudofermion fields χ : [89]:

$$\det M' = \int \mathcal{D}\chi^\dagger \mathcal{D}\chi e^{-\chi^\dagger M'^{-1}\chi}\,, \tag{2.50}$$

where the relation holds if the operator M' is positive definite. The simplest way to ensure positiveness is to use the square of the Dirac operator: $M' = M^\dagger M$ and thus the fermions then come in degenerate pairs. This forces the number of fermions in the theory to be even.

In order to evaluate the fermions in the HMC algorithm, we must invert the Dirac matrix M' and sample the pseudofermion fields χ. First, to invert the Dirac matrix, we use the conjugate gradient method [90]. Since the Dirac matrix can be large and sparse, the conjugate gradient is often the most expensive part of the simulation. The efficiency of the conjugate gradient method can be estimated with the condition number $\kappa = \lambda_{\max}/\lambda_{\min}$, where λ are the eigenvalues of the original matrix. Secondly, to sample the pseudofermion fields χ, we do a change of variables $\chi = M^\dagger \xi$:

$$\int d\chi d\chi^\dagger e^{-\chi (M^\dagger M)^{-1}\chi} = \det(M^\dagger M) \int d\xi d\xi^\dagger e^{-\xi^\dagger \xi}\,, \tag{2.51}$$

whence it follows, that by sampling ξ from complex Gaussian distribution we obtain $\chi = M^\dagger \xi$.

In order to further speed up the simulation code, the matrix M can be preconditioned [91] with the intent of reducing the condition number. For preconditioning we will introduce the Even-odd method [92, 93], where the lattice is divided into even and odd sites enumerated in such a way that the odd sites come first. The quark matrix M (2.40) can then be written in a block form:

$$M = \begin{pmatrix} A_o & -\kappa \not{D}_{oe} \\ -\kappa \not{D}_{eo} & A_e \end{pmatrix}\,, \tag{2.52}$$

where A and $-\kappa \not{D}$ blocks refer to the $\delta_{x,y}$ and κ parts in the definition of M^{clover} (2.40) respectively. Furthermore, we can write M as a Schur decomposition $M = LDU$ with:

$$L = \begin{pmatrix} 1 & 0 \\ -\kappa \not{D}_{eo} A_o^{-1} & 1 \end{pmatrix}\,, \quad D = \begin{pmatrix} A_o & 0 \\ 0 & M_e \end{pmatrix}\,, \quad U = \begin{pmatrix} 1 & -\kappa A_o^{-1} \not{D}_{oe} \\ 0 & 1 \end{pmatrix}\,, \tag{2.53}$$

where

$$M_e = A_e - \kappa^2 \not{D}_{eo} A_o^{-1} \not{D}_{oe} \,. \tag{2.54}$$

In this form the fermion action can be rewritten as:

$$\bar{\psi} M \psi = \bar{\psi}'_e M_e \psi'_e + \mathrm{Tr} \, \ln A_o \,, \tag{2.55}$$

where the fields have been redefined as $\psi' = U\psi$ and $\bar{\psi}' = \bar{\psi} L$, and ψ'_e are evaluated only on even sites. A_o depends only on the gauge fields and the condition number of M_e will be roughly half of the original matrix M, which directly leads to increased performance.

Another performance trick, that we can do on top of the even-odd preconditioning, is the Hasenbusch preconditioning [94, 95]. In the Hasenbusch preconditioning the determinant of a matrix M is written as:

$$\begin{aligned} \det(M^\dagger M) &= \det(W^+ W^-) \frac{\det(M^\dagger M)}{\det(W^+ W^-)} \\ &= \int \mathcal{D}\phi^\dagger \mathcal{D}\phi e^{-\phi_1^\dagger \frac{1}{W^+ W^-} \phi_1 - \phi_2^\dagger W^+ \frac{1}{M^\dagger M} W^- \phi_2} \,, \end{aligned} \tag{2.56}$$

where the matrices $W^\pm$ can be freely chosen, but naturally one should choose the matrices in such a way that the simulation becomes cheaper. One choice [96] is to choose $W^+ W^- = M^\dagger M + \mu^2$ with $\mu^2 = \sqrt{\lambda_{\max} \lambda_{\min}}$, where $\lambda_{\max/\min}$ are again the maximal and minimal eigenvalues of $M^\dagger M$. This procedure reduces the condition number of the fermion matrix to $\sqrt{\kappa}$.

2.7 Smearing

In the strong coupling regime, a lattice field theory can have a nonphysical bulk phase transition. This first order phase transition causes both the fermion mass and plaquette expectation value to have a significant discontinuity. Since the location of this transition depends on both the hopping parameter, which is used to tune the mass, and the bare coupling, the transition might happen at a vanishing PCAC mass and render massless simulations impossible in the high coupling region.

In [97] it is noted that combining the normal (unsmeared) gauge action with a gauge action calculated with smeared links will reduce discretization effects and move the bulk phase transition to higher couplings. The smeared links are fat links created by summing over the staples. This process is illustrated in figure 2.3. We mix the smeared and unsmeared gauge actions with a mixing coefficient c_g:

$$(1 - c_g) S_{\mathrm{G}}(U) + c_g S_{\mathrm{G}}(V) \,, \tag{2.57}$$

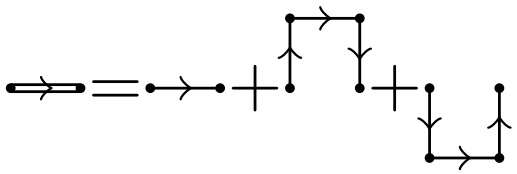

Figure 2.3: A schematic of fat link creation process using the staples on a two dimensional lattice.

where S_{G} is the Wilson gauge action (2.26), and U and V are the unsmeared and smeared gauge links respectively. We empirically set the mixing parameter to $c_g = 0.5$.

The common smearing methods are the Stout smearing [98], the HYP smearing [99] and the HEX smearing [76]. Out of these methods, we will focus on the HEX smearing, which combines properties of the HYP and Stout smearing. In HEX smearing the smeared links are calculated three times. Similarly to the HYP smearing, only the staples that are orthogonal to previous step are taken into account in each iteration:

$$\bar{V}_{x,\mu;\nu,\rho} = \mathrm{P}\left(\frac{\alpha_3}{2}\sum_{\pm\eta\neq\mu,\nu,\rho} U_{x,\eta}U_{x+\hat{\eta},\mu}U^{\dagger}_{x+\hat{\mu},\eta}U^{\dagger}_{x,\mu}\right)U_{x,\mu} \tag{2.58}$$

$$\tilde{V}_{x,\mu;\nu} = \mathrm{P}\left(\frac{\alpha_2}{4}\sum_{\pm\rho\neq\mu,\nu} \bar{V}_{x,\rho;\nu,\mu}\bar{V}_{x+\hat{\rho},\mu;\nu,\rho}\bar{V}^{\dagger}_{x+\hat{\mu},\rho;\mu,\nu}U^{\dagger}_{x,\mu}\right)U_{x,\mu} \tag{2.59}$$

$$V_{x,\mu} = \mathrm{P}\left(\frac{\alpha_1}{6}\sum_{\pm\nu\neq\mu} \tilde{V}_{x,\nu;\mu}\tilde{V}_{x+\hat{\nu},\mu;\nu}\tilde{V}^{\dagger}_{x+\hat{\mu},\nu;\mu}U^{\dagger}_{x,\mu}\right)U_{x,\mu}\,, \tag{2.60}$$

where:

$$\mathrm{P}(U) = \exp\left[U + U^{\dagger} - \frac{1}{2}\mathrm{Tr}\,(U - U^{\dagger})\right]\,, \tag{2.61}$$

and the matrix exponent is calculated using the Cayley-Hamilton theorem similarly to the stout smearing process. The coefficients α_i can be determined by maximizing the expectation value of the smeared plaquette $\langle \mathrm{Tr}\,(V_{\mu\nu})\rangle$. We will use the values for SU(2) model measured in [100]: $\alpha_1 = 0.78$, $\alpha_2 = 0.61$, and $\alpha_1 = 0.35$. Alternatively one could relate α_i's to similar coefficients in HYP smearing as: $(\alpha_1^{\mathrm{HYP}}, \alpha_2^{\mathrm{HYP}}, \alpha_3^{\mathrm{HYP}}) = (6\alpha_1^{\mathrm{HEX}}, 4\alpha_2^{\mathrm{HEX}}, 2\alpha_3^{\mathrm{HEX}})$, and then use the coefficients derived for QCD in [99]: $\alpha_1^{\mathrm{HEX}} = 0.125$, $\alpha_2^{\mathrm{HEX}} = 0.15$, and $\alpha_1^{\mathrm{HEX}} = 0.15$.

Chapter 3

Infrared behavior of the SU(2) gauge theory

3.1 Motivation

One of the stepping stones towards the Beyond the Standard Model lattice gauge theory is to determine the vacuum phase of the massless $SU(N_c)$ theories. Especially interesting is the question about the location of the lower boundary of the conformal window and the properties of the IRFP in theories within the conformal window. For recent reviews on these topics, we refer the reader to [101–103].

In this thesis we focus on the infrared properties of the $SU(2)$ gauge models with massless fermions. A much studied benchmark is the model with two adjoint fermions [75, 100, 104–116], which lattice studies have shown to be conformal. The lower boundary of the conformal window in the $SU(2)$ model with fundamental fermions is less clear. The two fermion case is perturbatively known to be confining and forms a novel dark matter candidate [117, 118]. For the four fermion case, we know from previous lattice studies [119] that this model is also confining. Likewise, we know from simulations that the ten fermion case [119] is conformal and has Banks-Zaks IRFP. The $SU(2)$ model loses asymptotic freedom at $N_f = 11$. For the models with $N_f = 6$ and $N_f = 8$, the previous studies on the lattice have given inconclusive results [119–123].

Knowing the infrared properties of these two models would be important for the conformal structure as the perturbative approximations estimate the lower boundary of the conformal window to be around six or eight fermions. The 2-loop scheme independent β-function predicts the lower boundary to be (1.36) at $N_f \approx 5.56$, the 3 and 4-loop expansions in $\overline{\text{MS}}$ scheme predict: $N_f \approx 3.9$ and $N_f \approx 5.9$ respectively [24, 25], the all-order-beta-function [44] predicts $N_f \approx 4.68$, the APC conjecture [41] predicts $N_f \approx 4.74$, and the ladder approximation [40]

predicts $N_f \approx 7.86$. All these estimates have a non-integer number of fermions, which should be understood so that when $N_f < N_f^{\text{boundary}}$, theory is confining. The 5-loop $\overline{\text{MS}}$ expansion [28] does not have an IRFP at $N_f = 6$ or $N_f = 8$, but instead it develops two separate conformal windows $3.0 \lesssim N_f \lesssim 5.8$ and $8.6 \lesssim N_f < 11$. This kind of behaviour is clearly unphysical, and shows that perturbation theory cannot be quantitatively relied upon when the fixed point appears at strong coupling.

We have run extensive simulations on both $N_f = 6$ [2] and $N_f = 8$ [1] and in section 3.5 we will confirm the existence of IRFP on both models at large gauge couplings. We also present the measurements of the two scheme independent quantities at the IRFP: the mass anomalous dimension γ_m^* [1,2] in section 3.7 and the leading irrelevant exponent of the coupling γ_g^* [3] in section 3.6. For these models, γ_g^* has never been measured before, and the mass anomalous dimension γ_m^* only has a previous measurement for the six fermion theory [119–121].

3.2 Gradient flow coupling

In recent years, the Yang-Mills gradient flow [124–127] has become the leading method of measuring the gauge couplings on the lattice. The success of the gradient flow algorithm is based on the increased accuracy with less statistics on larger lattices compared to the previously popular method of measuring the coupling using the Schrödinger functional with background fields [128,129]. Alongside with the coupling, the gradient flow also allows one to: perform a scale setting [130], measure the topological susceptibility [131] and other gauge invariant lattice operators, and measure the energy momentum tensor [132].

The basic idea of the gradient flow is to study the evolution of the field under the equation:

$$\partial_t B_{t,\mu} = -g_0^2 \frac{\delta S_{\text{YM}}}{\delta B_{t,\mu}} = D_{t,\nu} G_{t,\nu\mu} \tag{3.1}$$

$$B_{0,\mu} = A_\mu \tag{3.2}$$

$$G_{t,\mu\nu} = \partial_\mu B_{t,\nu} - \partial_\nu B_{t,\mu} + [B_{t,\mu}, B_{t,\nu}]\,, \tag{3.3}$$

where we have introduced a fictitious flow time coordinate t, $S_{\text{YM}} = \frac{1}{g_0^2} G_{\mu\nu} G^{\mu\nu}$ is the Yang-Mills action, and A_μ is the original gauge field. By driving gauge field along the deepest descent path towards the minima of Yang-Mills action, the gradient flow acts as a smoothing transformation and continuously removes the UV divergences. In the lattice formulation the continuum flow field is replaced by

the link variables $U_\mu(x,t)$ and evolved with the differential equation:

$$\frac{\partial}{\partial t}U_\mu(x,t) = -g_0^2 \left(\frac{\partial}{\partial U_\mu(x,t)} S_{\mathrm{GF}}[U]\right) U_\mu(x,t)\,, \tag{3.4}$$

where the initial condition is $U_\mu(x,0) = U_\mu(x)$. The lattice discretization of S_{GF} may be chosen independently of the action used in the simulation of the HMC evolution, and in this work we mostly use the Lüscher-Weisz action (2.42), but occasionally compare it to the plain Wilson action. When the Wilson gauge action is used, the gradient flow algorithm is often called the Wilson flow.

In order to show some properties of the gradient flow, we will sketch the perturbative solution of the continuum flow quantities presented fully in [126]. For the duration of the perturbative calculation we scale the gauge potential by the bare coupling $A_\mu \to g_0 A_\mu$, which allows us to expand the integrated flow equation in terms of g_0. To simplify these perturbative calculations we consider a modified flow equation:

$$\partial_t B_\mu = D_\nu G_{\nu\mu} + \lambda D_\mu \partial_\nu B_\nu\,, \tag{3.5}$$

where the free parameter λ is related to a gauge transformation:

$$B_\mu = \Lambda B_{\mu,\lambda=0}\Lambda^{-1} + \Lambda\partial_\mu\Lambda^{-1}\,, \quad \partial_t\Lambda = -\lambda\partial_\nu B_\nu\Lambda\,, \quad \Lambda_{t=0} = 1\,. \tag{3.6}$$

The choice $\lambda = 1$ tends to make calculations easier. Now, expanding the gauge field in terms of the bare coupling g_0: $B_\mu = \sum g_0^k B_{\mu,k}$, the modified flow equation becomes the heat equation for the first order of the expansion $k = 1$:

$$\partial_t B_{\mu,1} = \partial_\nu\partial_\nu B_{\mu,1}\,, \tag{3.7}$$

which can be solved using a heat kernel in momentum space [126]:

$$\begin{aligned} B_{\mu,1}(t,x) &= \int d^d y\, K_t(x-y) A_\mu(y) = \iint d^d y\, \frac{d^d p}{(2\pi)^d} e^{ip(x-y)} e^{-tp^2} A_\mu(y) \\ &= \int d^d y\, \frac{e^{-\frac{(x-y)^2}{4t}}}{(4\pi t)^{\frac{d}{2}}} A_\mu(y)\,. \end{aligned} \tag{3.8}$$

From this equation we can directly see that the gradient flow indeed smears the gauge field over a d-dimensional spherical volume of radius $\sqrt{8t}$. This is schematically shown in figure 3.1.

Now that we have the leading order expansion for the gradient flow, we would like to examine the energy density operator:

$$E = \frac{1}{4} G_{\mu\nu} G_{\mu\nu}\,. \tag{3.9}$$

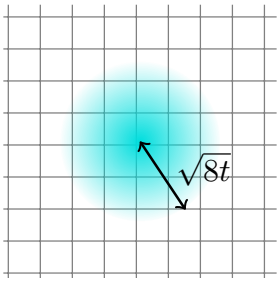

Figure 3.1: Gradient flow smears the lattice over a radius of $\sqrt{8t}$.

Similarly to the flow action, the discretization of the energy density can be chosen freely. We will mainly use the symmetric clover discretization (2.37) and the simple plaquette discretization (2.18). In the leading order, the expectation value of the energy density can be solved with the heat kernels as [126]:

$$\begin{aligned}\langle E\rangle &= \frac{1}{2}\langle \partial_\mu B_\nu \partial_\mu B_\nu - \partial_\mu B_\nu \partial_\nu B_\mu\rangle \\ &= \frac{1}{2} g_0^2 \langle \partial_\mu B_{\nu,1} \partial_\mu B_{\nu,1} - \partial_\mu B_{\nu,1} \partial_\nu B_{\mu,1}\rangle \\ &= \frac{1}{2} g_0^2 (N_c^2-1) \int_p e^{-2tp^2} (p^2\delta_{\mu\nu} - p_\mu p_\nu) D(p)_{\mu\nu} \\ &= \frac{1}{2} g_0^2 \frac{N^2-1}{(8\pi t)^{\frac{d'}{2}}} (d'-1) \left(1 + g_0^2 (2t)^\varepsilon \frac{\Gamma(2-2\varepsilon)}{\Gamma(2-\varepsilon)} \omega_1 + \cdots\right) ,\end{aligned} \tag{3.10}$$

where $D(p)_{\mu\nu}$ is the unrenormalized full gluon propagator:

$$D(p)_{\mu\nu} = \frac{1}{(p^2)^2} \left[\left(p^2\delta_{\mu\nu} - p_\mu p_\nu\right) \left(1 - \sum_{k=1}^{\infty} g_0^{2k} (p^2)^{-k\varepsilon} \omega_k\right)^{-1} + p_\mu p_\nu \right] , \tag{3.11}$$

$d' = 4-2\varepsilon$, ε is the dimensional regularization parameter, and ω_1 can be computed from the gluon self energy as:

$$\omega_1 = \frac{1}{16\pi^2} \left(4\pi e^{-\gamma_\mathrm{E}}\right)^\varepsilon \left[N \left(\frac{5}{3\varepsilon} + \frac{31}{9}\right) - N_f \left(\frac{2}{3\varepsilon} + \frac{10}{9}\right) + \mathcal{O}(\varepsilon) \right] , \tag{3.12}$$

where γ_E is the Euler's constant. It turns out that when we write the bare coupling g_0 in terms of the renormalized coupling g in the $\overline{\mathrm{MS}}$ scheme, the $1/\varepsilon$ divergences in g and $\langle E\rangle$ cancel each other and we can measure the renormalized coupling directly with the gradient flow. This automatic renormalization is a property of all composite gauge invariant observables [133, 134]. The perturbative expansion of $\langle E\rangle$ is known up to the NNLO level [135].

At leading order the gradient flow coupling at scale μ is given as:

$$g_{\mathrm{GF}}^2(\mu) = \mathcal{N}^{-1} t^2 \langle E\rangle|_{t=\frac{1}{8\mu^2}} , \quad \text{where} \qquad \mathcal{N} = \frac{3(N_c^2-1)}{128\pi^2} . \tag{3.13}$$

On the lattice, the normalization constant $\mathcal{N}$ depends on the choice of scale μ and gains additional contributions from finite size effects [136–138] and from the boundary conditions [139–142]. For this work, we will use the finite lattice Schrödinger functional result for $\mathcal{N}$ from [140]. Since the Schrödinger functional breaks translation invariance, we also need to change the definition of gradient flow coupling so that we only measure the coupling along a fixed time slice. The usual choice is the middle time slice $x_0 = L/2$, as it should have the smallest boundary effects.

The gradient flow comes with a natural scale $\mu = 1/\sqrt{8t}$. While the flow time t can be chosen freely, the lattice artifacts will make some choices of t to give more precise measurement of the coupling. In general, for the coupling to be free of both lattice artifacts and finite volume effects, we want to limit the scale into the regime $1/L \ll \mu \ll 1/a$ [127]. This can be done by relating the lattice scaling to the renormalization scale with a dimensionless parameter c_t [136, 137, 140]:

$$c_t L = \mu^{-1} = \sqrt{8t}\,. \tag{3.14}$$

A choice of constant c_t corresponds to the choice of scheme and only scheme independent quantities will agree if simulations with two separate c_t are compared. The constant c_t also sets the smoothing radius, so that at $c_t = 0.5$ the smoothing radius of the gradient flow is $L/2$ and we will effectively be smoothing over the whole lattice. This also implies that the larger c_t will be more subject to boundary effects. To choose the optimal c_t for each simulation, there are a couple of guidelines. Firstly, it is noted in [140] that for the Schrödinger functional boundary conditions the cutoff- and boundary effects and statistical variance are reasonably small within the range $0.3 < c_t < 0.5$. Secondly, since we want to choose a c_t that minimizes the lattice effects, one must compare different discretizations and see that they give the same continuum limit [127, 143]. Overall, the choice of c_t is a compromise between reduced cutoff effects, which are smallest at large c_t, and statistical variance, which tends to grow as c_t grows.

Regardless of the choice of c_t the flow and the measured quantities will come with a discretization error, which was quantified at [126] to be of order $\mathcal{O}(a^2)$. Therefore, the gradient flow coupling can be expanded as:

$$g^2_{\mathrm{GF}} = \mathcal{N}^{-1} t^2 \langle E(t) \rangle|_{c_t L = \sqrt{8t}} = \left(\frac{a}{L}\right)^2 A(c, L) + \mathcal{O}(a^4)\,. \tag{3.15}$$

In order to improve the gradient flow measurement, one could do a full Symanzik type analysis, which will then lead to the Zeuthen flow [144]. The Zeuthen flow is a fully $\mathcal{O}(a^2)$ improved version of the gradient flow and has been applied to coupling measurements in [145]. Furthermore, a $\mathcal{O}(a^4)$ improvement was first

suggested in [146]. These improvements are, however, mostly derived for other boundary conditions than the Schrödinger functional and therefore we will focus on phenomenological improvements.

The gradient flow $\mathcal{O}(a^2)$ effect can be significantly reduced by using tunable modifications to the coupling measurement. The first such modification is the τ-correction [147], in which we shift the time of energy density measurement by τ_0:

$$g^2_{\mathrm{GF}} = \mathcal{N}^{-1}t^2\langle E(t+\tau_0)\rangle = \mathcal{N}^{-1}t^2\langle E(t)\rangle + \mathcal{N}^{-1}t^2\left\langle \frac{\partial E(t)}{\partial t}\right\rangle \tau_0 a^2 + \mathcal{O}(a^4)\,. \quad (3.16)$$

Now the value of τ_0 has to be tuned by hand in such a way that $A(c, L)$ from Eq. (3.15) is removed. We describe the tuning process we use in the section 3.5.

Another way to improve the gradient flow coupling measurement is to note that different discretizations used in the simulation, flow, and energy density, will have different finite size effects. If we combine any two measurements done with different lattice discretizations, with a mixing factor X, we can make their $\mathcal{O}(a^2)$ effects cancel each other. The simplest choice is to combine clover and plaquette measurements of the energy density:

$$g^2_{\mathrm{GF}} = \mathcal{N}^{-1}t^2\left[(1-X)\langle E_{\mathrm{Clover}}(t)\rangle + X\langle E_{\mathrm{Plaq.}}(t)\rangle\right]\,. \quad (3.17)$$

The coefficient X can be tuned either by hand or calculated perturbatively. The perturbative result [138, 146] is:

$$X = 1 - 6\left(2c_f + \frac{2}{3}c_g + \frac{1}{8}\right)\,, \quad (3.18)$$

where c_g and c_f are the rectangle coefficients (2.42) for the simulation action and the flow action respectively. For the Lüscher-Weisz flow we would have $X = 1.25$.

3.3 Freezing of the topology

The Yang-Mills theory on a periodic lattice forms a torus and carries an integer topological number Q. In the continuum, this topological instanton number always has an integer value, but on the lattice Q is a continuous variable that gets more discrete features as the continuum is approached. Near the continuum, the topological charges will separate the otherwise connected gauge field configurations into fixed topological sectors. The probability distribution of these sectors should form a Gaussian shaped histogram, but in some circumstances the gauge field can get trapped inside a fixed topological sector. When this happens the topology stays at the same value for an extended period of the simulation time and the

topology is said to be frozen. This freezing will cause undersampling of the real topological number and can lead to extended autocorrelations [148, 149] and biased numerical results in other measurements such as the gradient flow coupling. In [150] it is observed that high amounts of configurations with non-vanishing topological charge that are not balanced by equivalent negative charge, will lead to unnaturally high gradient flow coupling results.

With the gradient flow method, we can measure the topological charge density without additional computational cost:

$$Q(t) = \frac{1}{32\pi^2} \sum_x \epsilon_{\mu\nu\alpha\beta} G^a_{\mu\nu}(x,t) G^a_{\alpha\beta}(x,t)\,, \tag{3.19}$$

for a large enough flow time t. Alike to the energy density, this quantity is automatically renormalized by the gradient flow procedure. We measure this quantity from our configurations [1, 2] and show in figure 3.2 some example cases of topological behavior we run into. At the small lattice couplings, indicated by the large $\beta_L \sim 8$, the topology is frozen to zero and no problems occur. Likewise, at large couplings, the topology fluctuates freely around zero with roughly symmetrical distribution, with equal amount of positive and negative topological charges and again we observe no problems. However, the problems arise in the intermediate region of lattice couplings where the topology is barely fluctuating. Within this region we observe the freezing of the topology and the tunneling probability from one topological sector to another decreases, which increases the autocorrelation times and gives biased coupling measurements as discussed earlier. The remedy is, that the simulation seems to tunnel into the well behaving zero topology region more often than it tunnels out of it. This allows us to wait until the simulation is fully frozen into the zero topology sector and start the measurements there. We effectively restrict the freezing to non-zero topology to the thermalization phase of the simulation.

An alternative solution would be to restrict the simulation at all couplings to the zero topology [145, 150] during the data-analysis. In our case this is not feasible as the topology fluctuates so much at the large lattice couplings that we would have to reject almost all measurements.

3.4 Simulations of SU(2) with $N_f = 6$ and $N_f = 8$

We run simulations on the $SU(2)$ gauge model with $N_f = 6$ and $N_f = 8$ massless Dirac fermions in the fundamental representation [1,2]. Of the simulation methods introduced in the section 2.1, our simulation code uses the hybrid Monte Carlo

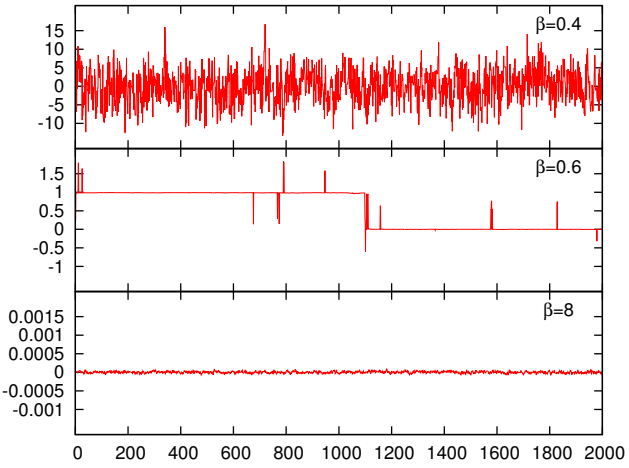

Figure 3.2: Freezing of topology at $N_f = 8$ model with different values of β_L.

algorithm with a 2nd order Omelyan integrator and chronological initial values for the fermion matrix solution vector. We take the trajectory length to be 1 and adjust the step length in the HMC algorithm so that the Metropolis algorithm acceptance rate is greater than 80%. The fermions are preconditioned using the even-odd preconditioning and Hasenbusch preconditioning as explained in the section 2.6.

For actions we use the partially smeared plaquette gauge action together with the clover improved fermion action from the section 2.4. We choose the mixing parameter to be $c_g = 0.5$ and the Sheikholeslami-Wohlert coefficient to be $c_{sw} = 1$, which is the standard choice for smeared clover fermions [75–77] and was verified in earlier studies [119, 151] to give the right correction for our action. The smearing is implemented with the HEX-smearing using the smearing coefficients from [100]. We use the Schrödinger functional boundary conditions with Dirichlet boundaries and set the boundary improvement $c_t = 1$. The smearing was fully discussed in the section 2.7 and the boundary conditions in the section 2.5.

We carry out the simulations with a varying number of bare couplings $g_0^2 = 4/\beta_L$ with β_L varying from $\beta_L = 8$ to $\beta_L = 0.5$ for $N_f = 6$ and $\beta_L = 0.4$ for $N_f = 8$. The smallest achievable β_L is limited by the onset of bulk phase transition on bare couplings larger than the ones used. We use lattice sizes $L = 8, 10, 12, 16, 18, 20, 24, 30$ for the $N_f = 6$ model and $L = 6, 8, 10, 12, 16, 20, 24, 32$ for the $N_f = 8$ model. We tune the fermion masses to zero by finding the value of $\kappa_c(g_0^2)$ of the hopping parameter at which the PCAC mass (2.49) vanishes. In order to find the value of $\kappa_c(g_0^2)$, we measure the PCAC mass at multiple hopping parameter values and interpolate to vanishing mass. We do this interpolation

$N_f = 6$

β_L	κ_c	β_L	κ_c	β_L	κ_c
8	0.125310366353981	1.5	0.128799165934744	0.6	0.136438136224601
6	0.125459579958083	1.3	0.129603737388233	0.55	0.137424583321490
4	0.125860459184944	1	0.131448889150607	0.53	0.137839481272905
3	0.126367585261215	0.9	0.132331360707040	0.5	0.138504981089103
2	0.127533813721664	0.8	0.133419041876613		
1.7	0.128194200995596	0.7	0.134765027707880		

$N_f = 8$

β_L	κ_c	β_L	κ_c	β_L	κ_c
8	0.125307435050069	1.7	0.127885967693622	0.7	0.132608779236301
6	0.125452134243701	1.5	0.128375672766415	0.6	0.133664962983886
5	0.125590630318978	1.3	0.129010604974215	0.55	0.134267867684544
4	0.125833726509734	1	0.130374869159002	0.5	0.134939416622759
3	0.126301695421514	0.9	0.130990832298533	0.45	0.135670680413224
2	0.127329165457485	0.8	0.131727494527597	0.4	0.136470043334909

Table 3.1: Values of the critical hopping parameter κ_c for $N_f = 6$ and $N_f = 8$.

procedure for each β_L, but only for the $L = 24$ sized lattices. We then proceed to use the same $\kappa_c(g_0^2)$ for all the other lattice sizes, which means that our smaller lattices develop a small mass and lattices greater than $L = 24$ develop a small and negligible negative mass of order 10^{-5}. The values of κ_c used in both models are reported in the table 3.1.

We thermalize the configurations and take the topology freezing into account. After these we measure the gradient flow coupling. We choose $c_t = 0.3$ for $N_f = 6$ and $c_t = 0.4$ for $N_f = 8$ for the bulk of the study. The number of measured trajectories is in the range: 10^4–10^5, where generally the larger more expensive lattices have somewhat smaller statistics than the cheap small ones. The coupling is measured with the gradient flow method (3.13) and the results are shown in figure 3.3, where the errors are measured using the Jackknife procedure. It is evident from the figure that the finite size effects become substantial at large couplings. Because the finite size effects are stronger on smaller lattices, we limit our analysis to lattice sizes $L \geq 10$.

In the following sections, we present different observables as functions of the measured coupling g^2_{GF}. For this purpose we will make the coupling measurement

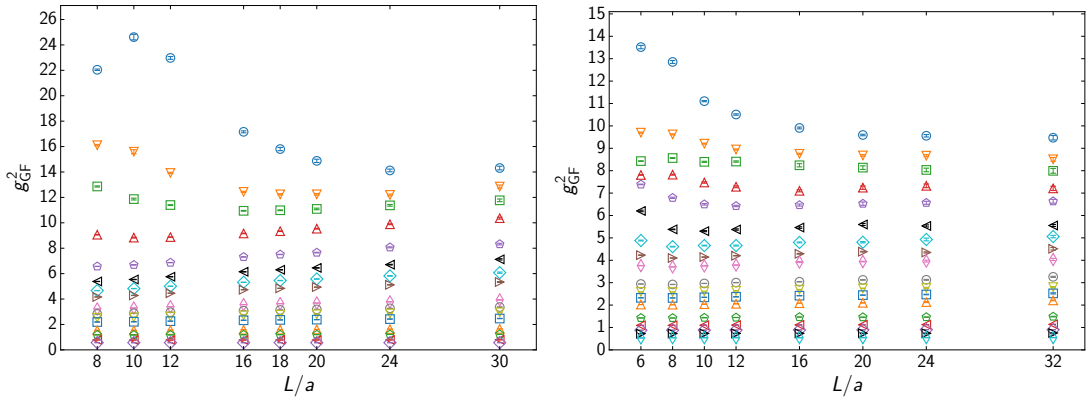

Figure 3.3: The raw gradient flow coupling measurements g^2_{GF} at each β_L and L on the lattice for the $N_f = 6$ theory (*left*) and for the $N_f = 8$ theory (*right*).

continuous by using an interpolation. For $N_f = 6$ the data is smooth enough to be interpolated with a polynomial function [2]:

$$g_{\mathrm{GF}}(g_0, a/L, t) = g_0^2(1 + \sum_{i=1}^{m} a_i g_0^{2i}) \,, \tag{3.20}$$

where we achieve the best possible fit when $m = 10$ for lattices $L < 16$ and $m = 9$ for larger lattices. The goodness of the fit is measured using the χ^2/d.o.f test, which will give results below 2 for the chosen polynomial ansatz. We also analyze the systematic error caused by the choice of the polynomial order by repeating the analysis with $m - 1$ and observing the changes. While χ^2/d.o.f slightly increases with smaller polynomial order, the interpolating curve stays compatible with the earlier result.

On the other hand, the $N_f = 8$ data is more non-linear, which makes a good polynomial fit a problem. Therefore we have decided to follow a rational ansatz. The rational fit function has been previously used in [100, 119, 152]. More precisely, the function is [1]:

$$g^2_{\mathrm{GF}}(g_0^2, L/a, t) = g_0^2 \frac{1 + \sum_{i=1}^{n} a_i g_0^{2i}}{1 + \sum_{j=1}^{m} b_j g_0^{2j}} \,, \tag{3.21}$$

where we have chosen $n = 7$ and $m = 1$ for the bulk of the analysis and test the systematics by varying both the n and m by 1. In the $N_f = 8$ case we decided to use same order functions for all lattice sizes and the optimal orders for the denominator and the numerator were found by both the χ^2/d.o.f test and using the leave-one-out cross validation method. In this model χ^2/d.o.f are slightly larger than in the $N_f = 6$ case, as they rise to 3.5 at maximum. While χ^2/d.o.f could be made lower by increasing the order of the fit function, such change

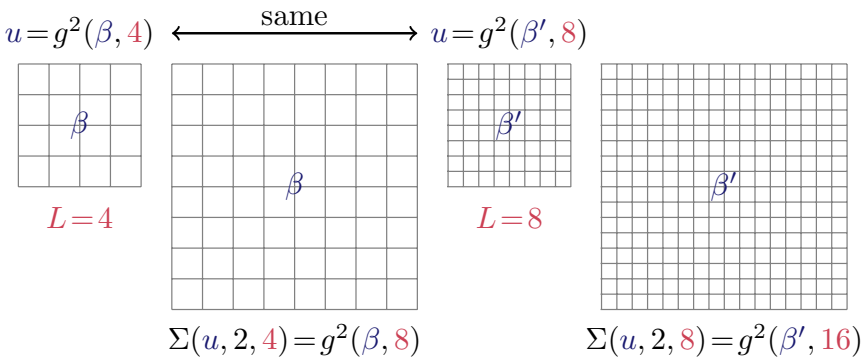

Figure 3.4: Schematic of the step scaling process (3.23) with $a = 1$.

would increase the risk of overfitting, which would lead to underestimation of the statistical errors. In fact, we will note in the section 3.6 that even the current choice might slightly overfit around the IRFP. However, the results obtained by the chosen fit ansatz are stable and reliable.

3.5 Running of the coupling

In order to quantify the running of the coupling by using the finite lattice spacing step scaling function [153]. If we write the β-function on the lattice as:

$$\beta(g) = -L\frac{\partial g}{\partial L}\,, \tag{3.22}$$

where the coupling is measured at scale $\mu \propto 1/L$, we can then find the coupling $g(sL)$ for arbitrary coefficient s by integrating the β-function with an initial value $g(L)$. This change in coupling, when lattice size is scaled from L to sL, is quantified by the step scaling function and is defined as:

$$\Sigma(u, s, L/a) = g^2(g_0^2, sL/a)|_{g^2(g_0^2, L/a)=u} \tag{3.23}$$

and is schematically presented in figure 3.4. While the s can be chosen freely, we choose $s = 3/2$ for the $N_f = 6$ and $s = 2$ for the $N_f = 8$, since with these choices we get the highest amount of possible lattice pairings in the set of simulated lattices.

The continuum version of the step scaling function can be defined as a limit:

$$\sigma(u, s) = \lim_{\frac{a}{L}\to 0} \Sigma(u, s, L/a)\,. \tag{3.24}$$

Since we are using actions and algorithms improved in the lattice spacing, we expect the errors to be of order $\mathcal{O}(a^2)$ and find the continuum step scaling function

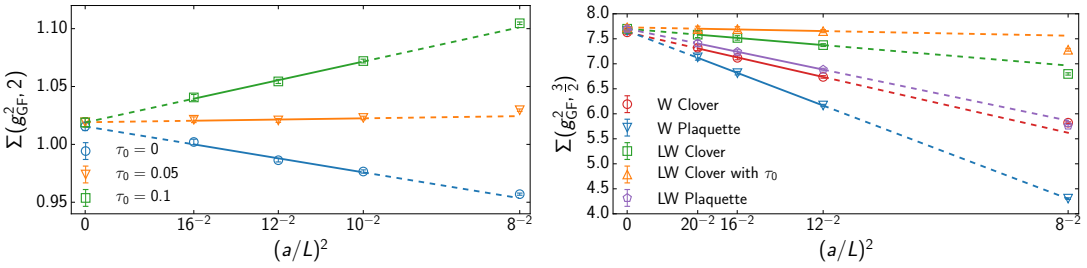

Figure 3.5: *Left:* The correct τ_0 value can be found by minimizing the slope of the a^2-scaling. *Right:* The a^2-scalings of different discretizations.

as a linear fit:

$$\Sigma(u, s, L/a) = \sigma(u, s) + c(u) \left(\frac{a}{L}\right)^2 . \tag{3.25}$$

The step scaling function is related to the β-function with relation:

$$\int_u^{\sigma(u,s)} \frac{\mathrm{d}x}{\sqrt{x}\beta(\sqrt{x})} = -2 \int_L^{sL} \frac{\mathrm{d}L}{L} = -2 \ln(s) , \tag{3.26}$$

and therefore allows us to measure the running of the coupling. Usually one studies the quantity Σ/g^2 instead of just the step scaling function by itself, since Σ/g^2 will run to unity at fixed points.

The step scaling function can also be used to tune the τ_0-correction from Eq. (3.16) and to quantify the discretization effects of different parameter choices. On the left hand side of figure 3.5 we see an example of the τ_0 tuning procedure for the $N_f = 8$ theory. We can see that by setting τ_0 to the optimal value, most of the $\mathcal{O}(a^2)$ effects will vanish. As the cutoff effects grow, the optimal τ_0 will also change. τ_0 should not depend on the bare couplings [127] as that would affect the matching procedure in the step scaling function. However, τ_0 can depend on the renormalized quantities, such as the gradient flow coupling g^2_{GF}. Since these quantities depend on τ_0 themselves, one must find the optimal τ_0-correction iteratively starting from the bare couplings. Another concern when τ_0 is made a function of the measured coupling, is the fact that τ_0 should be a small shift in the flow time and should be limited to $|\tau_0| \ll t/a^2$ region. With these restrictions, we have found a logarithmic form for the τ_0-correction to give the most satisfying results [1, 2]:

$$\tau_0 = \begin{cases} 0.025 \log(1 + 2g^2_{\mathrm{GF}}) & \text{for } N_f = 6 \\ 0.06 \log(1 + g^2_{\mathrm{GF}}) & \text{for } N_f = 8 . \end{cases} \tag{3.27}$$

These are tuned with $c_t = 0.3$ for $N_f = 6$ and $c_t = 0.4$ for $N_f = 8$. The τ_0 correction tuned for lower c_t can be used at higher c_t, since the discretization

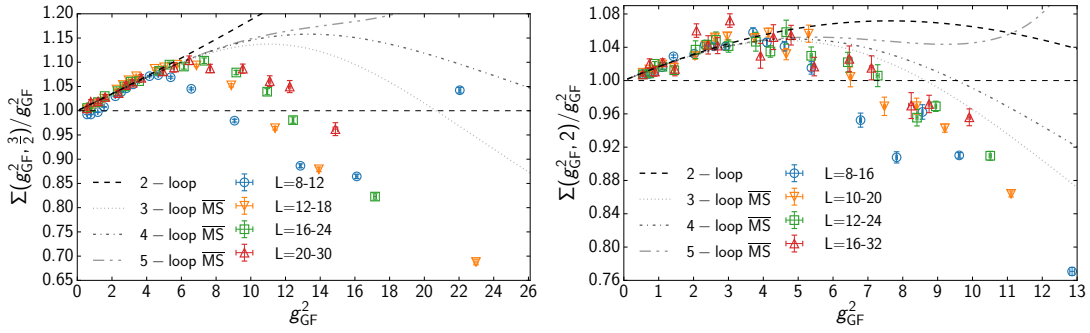

Figure 3.6: The lattice step scaling function (3.23) with the τ_0-correction (3.27) for the $N_f = 6$ theory (*left*) and for the $N_f = 8$ theory (*right*).

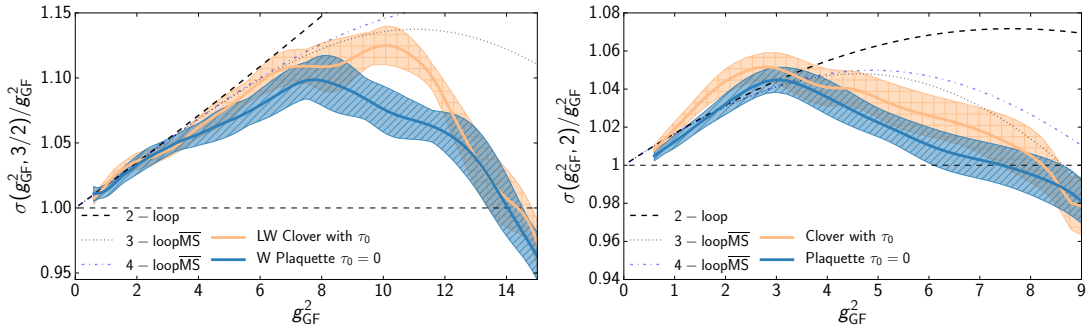

Figure 3.7: The continuum limit (3.25) of the lattice step scaling function shown in figure 3.6; for the $N_f = 6$ theory (*left*) and for the $N_f = 8$ theory (*right*). using two different discretization choices.

effects tend to grow along with c_t. However, trying to use τ_0 tuned for higher c_t at lower c_t can break the $|\tau_0| \ll t/a^2$ limit.

On the right hand side of figure 3.5 we study the different lattice discretizations. The main observation is that for the more improved actions, such as the Lüscher-Weisz and the Clover actions, we have smaller $\mathcal{O}(a^2)$ scaling than for less improved actions, such as the Wilson plaquette action. Because of this, we do the bulk of our analysis with the Lüscher-Weisz action and the clover definition of the energy density. Furthermore, we observe that at small couplings all the discretizations tried will give the correct continuum limit. At larger couplings, the continuum results of the discretizations will start to slightly separate, but the order of the results does not change, i.e. the less improved actions consistently give smaller continuum result than the more improved actions. This allows us to estimate the systematical errors of the results by comparing the less and most improved

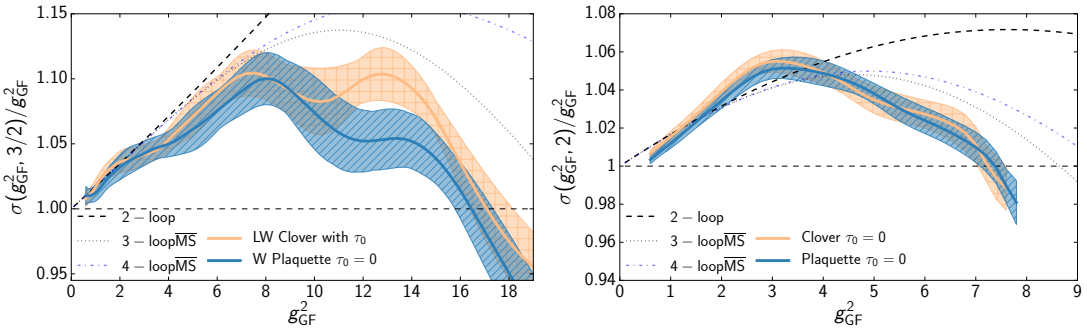

Figure 3.8: The continuum limit (3.25) of the lattice step scaling function at $c_t = 0.35$ for the $N_f = 6$ theory (*left*) and for the $N_f = 8$ theory (*right*).

continuum results.

In figure 3.6 we present the raw lattice step scaling function (3.23) calculated from the data shown in figure 3.3. We observe that for both cases $N_f = 6$ and $N_f = 8$, the running of the coupling is compatible with the 2-loop scheme independent perturbative curve up to intermediate couplings around $g^2_{\rm GF} \sim 6$. After this point, the lattice result deviates towards an IRFP. The higher order $\overline{\rm MS}$ curves are scheme dependent and cannot be directly compared to our result. Since the 5-loop $\overline{\rm MS}$ curve barely fits the figure, we will leave it out from all the figures to follow. The continuum extrapolation (3.25) of these two step scaling functions are presented in the figure 3.7. For $N_f = 6$ at the left side of figure, the errors include both the statistical errors and systematics rising from the interpolation, while the $N_f = 8$ side of figure only has statistical errors. For both $N_f = 6$ and $N_f = 8$, we show that the location of the fixed point does not depend on the chosen discretization. The discretizations shown, are chosen to differ from each other in their $\mathcal{O}(a^2)$ scaling as much as possible. We observe in figure 3.7 an IRFP at $g^2_* = 14.5(4)^{+0.4}_{-1.2}$ for $N_f = 6$ and $g^2_* = 8.24(59)^{+0.97}_{-1.64}$ for $N_f = 8$, where the first set of errors corresponds to the statistical errors and the second set of errors tell the variance of the result between different discretization choices [1, 2]. Finally, we show that the existence of the IRFP does not depend on the flow parameter c_t in figure 3.8, where both $N_f = 6$ and $N_f = 8$ continuum limits have shown at $c_t = 0.35$. Because, each c_t corresponds to a different renormalization scheme, the location of the IRFP moves to $g^2_* = 17.1(5)^{+0.8}_{-1.3}$ in the $N_f = 6$ model and to $g^2_* = 7.23(19)$ in the $N_f = 8$ model.

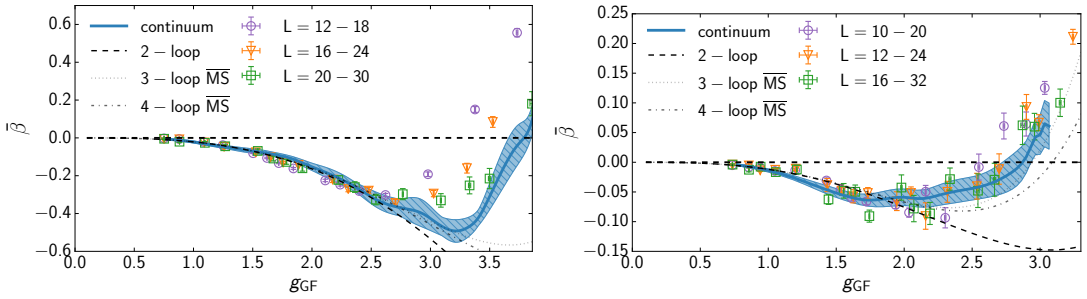

Figure 3.9: The $\bar{\beta}$-function (3.30) for the raw step scaling function (3.23) and its continuum extrapolation (3.25) for: *Left:* $N_f = 6$ *Right:* $N_f = 8$.

3.6 Leading irrelevant exponent of the coupling

We also measure the leading irrelevant exponent of the coupling γ_g^* at the IRFP:

$$\gamma_g^* = -\frac{\mathrm{d}\beta(g)}{\mathrm{d}g}\bigg|_{g=g_*} . \tag{3.28}$$

Recently this quantity has been estimated in a scheme-independent perturbative expansion [154, 155]. This expansion predicts $\gamma_g^* \sim 0.65$ for the $N_f = 6$ model and $\gamma_g^* \sim 0.25$ for the $N_f = 8$ model.

In order to measure γ_g^* on the lattice, we have to relate the step scaling result to the β-function with the relation (3.26). If we assume that the β-function is small at the IRFP $\beta(g) \sim 0$, and that the coupling runs slowly, we can approximate the integral as a Riemann sum:

$$\int_u^{\sigma(u,s)} \frac{\mathrm{d}x}{\sqrt{x}\beta(\sqrt{x})} = \frac{\sigma - u}{\sqrt{x}\beta(\sqrt{x})} = \frac{g}{\beta(g)}\left(\frac{\sigma}{g^2} - 1\right) = -2\ln(s)\,, \tag{3.29}$$

where, because of slow running, $\sqrt{x} = \sqrt{u} = g$. From here, we can solve the β-function in the vicinity of the IRFP in terms of the step scaling function:

$$\bar{\beta}(g) \equiv \frac{g}{2\ln(s)}\left(1 - \frac{\sigma(g^2, s)}{g^2}\right) . \tag{3.30}$$

While this equation is exact only in the limit $g \to g_*$, where $\beta(g_*) = 0$, the same formula can be derived by linearizing the β-function as $\beta(g) \approx \gamma_g^*(g - g_*)$, solving the integral (3.26), and Taylor expanding the result. Because of this, we can say that the slope of $\bar{\beta}$ should correspond to the slope of β-function.

In figure 3.9 we present the $\bar{\beta}$-function using the data from figures 3.6 and 3.7 [3]. We observe that even though the relation (3.30) is exact only at the IRFP, the data follows the 2-loop perturbative β-function nicely in the small coupling region. For the $N_f = 6$ model, $\bar{\beta}$ is well behaved around the IRFP and we can directly measure

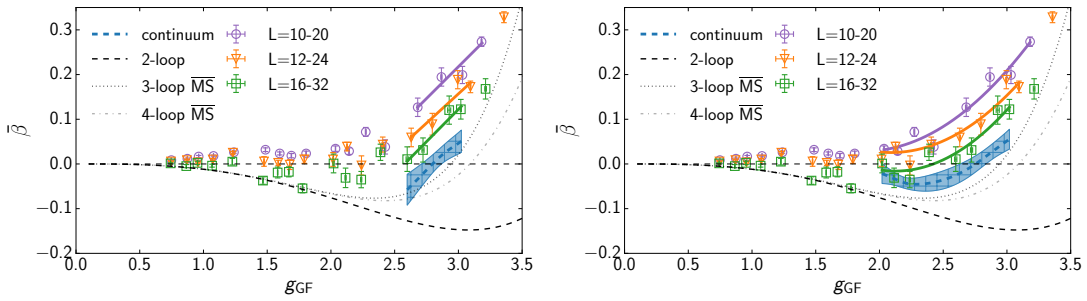

Figure 3.10: The raw step scaling function (3.23) and its continuum extrapolation (3.25) for $N_f = 8$ using: *Left:* Linear fit, and *Right:* quadratic fit.

the slope $\gamma_g^* = 0.648(97)^{+0.16}_{-0.1}$, where the first set of the errors correspond to the statistical error similar to figure 3.9 and the second set of errors give the variance between discretizations. The estimate from [154, 155] $\gamma_g^* \sim 0.65$ fits well within these measurements. The $N_f = 8$ model is trickier. The rational interpolation develops a curvature around the IRFP and makes a reliable measurement of γ_g^* impossible.

To alleviate the curvature at the IRFP, we will perform the interpolation directly in $\bar{\beta}$ instead of the couplings [3]. Similar methods have been used in [100, 116, 145]. As we are interested only on the behavior at the IRFP, we will limit our interpolation to points at large couplings. In figure 3.10 we show two examples: linear and quadratic fits for the $N_f = 8$ data without the τ-correction. Using the quadratic fit we can the measure the slope even for the $N_f = 8$ theory and get $\gamma_g^* = 0.19(8)^{+0.21}_{-0.09}$. where the first set of errors is the statistical error and the second set gives the variance between the discretizations. Here the discretization dependence is inspected using the discretization mixing coefficient X (3.17). In figure 3.11 we show that the continuum limit at the IRFP is stable with respect to the variations of X and that the measured γ_g^* value is stable between variations of X and fit functions. Again, the result agrees with the scheme independent estimate $\gamma_g^* \sim 0.25$ within the errors.

A similar analysis for $N_f = 6$ would result in the slope $\gamma_g^* = 0.66(4)^{+0.25}_{-0.13}$, which is well within the errors of the earlier measurement from the interpolated couplings. Re-doing the analysis with different values of the scheme changing parameter c_t will keep the results constant within the errors and prove the scheme independence of the results.

The above results rely on the assumption of a a^2-scaling at the IRFP. However, the Symanzik improvement program is based on arguments around the UV

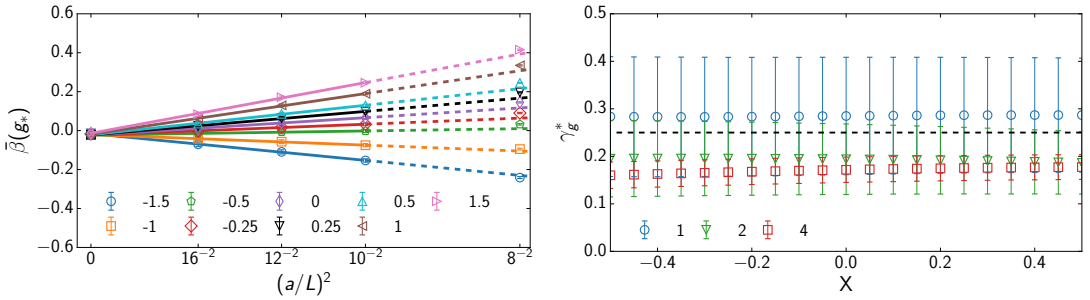

Figure 3.11: *Left:* The continuum limit at the IRFP for the $N_f = 8$ model at different values of X (3.17). *Right:* The measurement of γ_g^* for the $N_f = 8$ model with linear, quadratic, and quartic fits and varying X.

Gaussian fixed point and at the IRFP the scaling can be modified by nontrivial scaling exponents. If these scaling exponents remain small near the infrared fixed point, we can assume that the power counting argument holds and cutoff effects dominated by dimension 6 operators decrease with the power of lattice spacing a. Since we have checked our continuum limit with multiple different a^2 scalings by either varying X in Eq. (3.17) for $N_f = 6$ and $N_f = 8$, or by doing the analysis with multiple different discretizations for $N_f = 6$, and we have checked the scheme independence by varying the parameter c_t, we argue that the scaling violation is small and the continuum limit is robust [3].

However, the consistency of the a^2 continuum limit can be checked by also using an alternative method of measuring γ_g^*. The finite size scaling method developed in [143, 152, 156, 157], integrates the lattice β-function (3.22) linearized around the fixed point $\beta(g^2) = \gamma_g^*(g^2 - g_*^2)$:

$$g_{\mathrm{GF}}^2(g_0, L) - g_*^2 = \left[g_{\mathrm{GF}}^2(g_0, L_{\mathrm{ref}}) - g_*^2\right] \left(\frac{L_{\mathrm{ref}}}{L}\right)^{\gamma_g^*} . \tag{3.31}$$

This equation relies on the evolution of the coupling towards the fixed point as the lattice size is increased from L_{ref} to L. Hence, it cannot be used exactly at the fixed point where there is no evolution, but in some environment around it. We note that this also assumes vanishing discretization artifacts, and thus this method demands large lattices that are already close enough to the continuum.

In figure 3.12 we show the fit to Eq. (3.31) for the discrete values of β_L for both the six and eight flavor theories [2, 3]. As long as the L_{ref} is chosen to be sufficiently large and the β_L is not directly at the IRFP, the method behaves rather well. We then interpolate the couplings, with polynomial ansatz for $N_f = 6$ and rational ansatz for $N_f = 8$, to plot the figure 3.13. Due to this method being

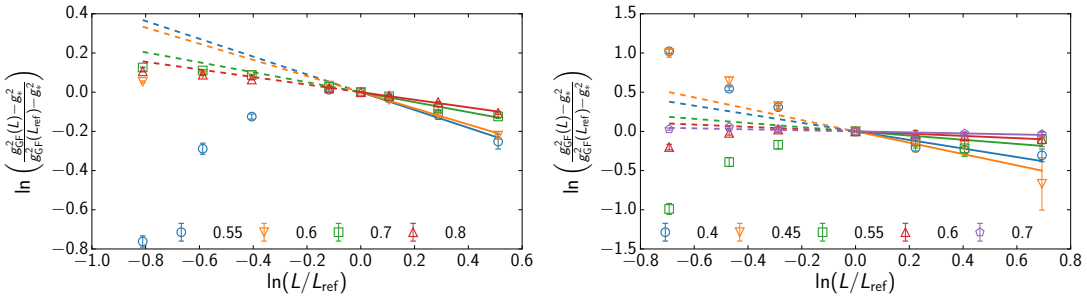

Figure 3.12: Fit to function (3.31) for measured couplings g^2_{GF} with τ_0-correction at: *Left:* $N_f = 6$ with $\beta_L = 0.55, \ldots, 0.8$ at $c_t = 0.3$, using $L_{\mathrm{ref}}/a = 18$; and *Right:* $N_f = 8$ with $\beta = 0.4, \ldots, 0.7$ at $c_t = 0.4$ using $L_{\mathrm{ref}}/a = 16$.

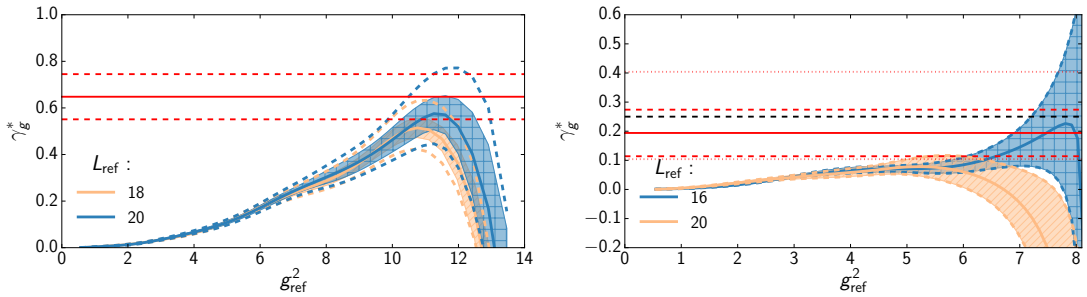

Figure 3.13: The interpolated version of the figure 3.12 for $N_f = 6$ (*Left*, the dashed bands indicate the variance of the g^2_*) and $N_f = 8$ (*Right*). The red bands show the result from the slope of the $\bar{\beta}$-function (3.30) and the black line shows the scheme invariant perturbative estimate.

unstable at the IRFP, we cannot quote an exact value of γ^*_g, but we observe that for both theories γ^*_g rises towards the values measured from the slope. Therefore, this method confirms the reliability of the measurement we got from the slope of the $\bar{\beta}$-function (3.30).

3.7 Mass anomalous dimension

We measure the mass anomalous dimension γ_m (1.27) using two different methods [1,2]: the mass step scaling method, which is enabled by the use of Schrödinger functional boundary conditions, and the spectral density method, which is based on the eigenvalue density of the Dirac operator.

In the step scaling method we write a step scaling function for the renormal-

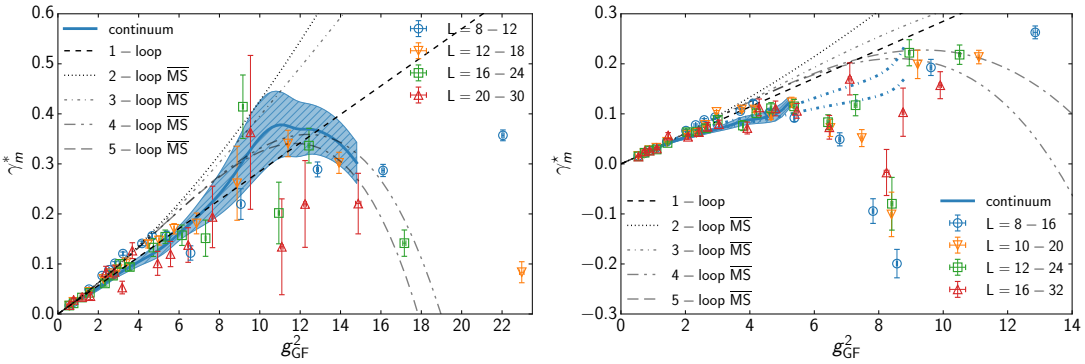

Figure 3.14: The mass anomalous dimension γ_m^* measured with the mass step scaling method. The data points show the raw data and the shaded band the continuum limit for *Left:* the $N_f = 6$ and *Right:* the $N_f = 8$. The dashed lines in the $N_f = 8$ figure, indicate the behavior of the continuum extrapolation if it is done in the unstable region.

ization constant Z_P (2.48) akin to the coupling step scaling function [86]:

$$\Sigma_P(u, s, L/a) = \left.\frac{Z_P(g_0, sL/a)}{Z_P(g_0, L/a)}\right|_{g^2(g_0, L/a)=u} \tag{3.32}$$

$$\sigma_P(u, s) = \lim_{a/L\to 0} \Sigma_P(u, s, L/a)\,, \tag{3.33}$$

where the continuum limit is taken by assuming linear scaling in a^2, and the scaling parameter s is chosen to be $s = \frac{2}{3}$ for the $N_f = 6$ and $s = 2$ for $N_f = 8$. In order to get a continuous dependence on $g^2_{\rm GF}$, we interpolate Z_P with the polynomial ansatz (3.20) with $m = 8$ for $N_f = 6$ and $m = 5$ for $N_f = 8$. The mass anomalous dimension γ_m is related to the mass step scaling function via the relation [158]:

$$\sigma_P(u, s) = \left(\frac{u}{\sigma(u, s)}\right)^{d_0/(2b_0)} \exp\left[-\int_{\sqrt{u}}^{\sqrt{\sigma(u,s)}} dx \left(\frac{\gamma_m(x)}{\beta(x)} - \frac{\gamma_0}{\beta_0 x}\right)\right], \tag{3.34}$$

where β_0 and γ_0 are the 1-loop coefficients defined in (1.33) and (1.35) respectively. Close to the IRFP, Eq. (3.34) simplifies to:

$$\log \sigma_P(g^2, s) \simeq -\gamma_m^*(g^2) \int_\mu^{s\mu} \frac{d\mu'}{\mu'} = -\gamma_m^*(g^2) \log s, \tag{3.35}$$

$$\Rightarrow \gamma_m^*(g^2) = -\frac{\log \sigma_P(g^2, s)}{\log s}\,. \tag{3.36}$$

While the above relation is exact and $\gamma_m^* = \gamma_m$ only at the IRFP, we will use it for all values of $g^2_{\rm GF}$.

Both the lattice step scaling measurement and its continuum limit for both $N_f = 6$ [2] and $N_f = 8$ [1] are shown in figure 3.14. We observe that even though the method is derived for couplings near the IRFP, it replicates the perturbative behavior at small couplings. At large couplings, this method seems to become unstable and a proper continuum extrapolation becomes difficult as the χ^2/d.o.f errors grow rapidly. In the $N_f = 6$ case a proper continuum limit can be achieved with increased errors, but for the $N_f = 8$ model, we decided to restrict the continuum limit into the region where the data behaves well.

On the other hand, the spectral density method is based on the fact that γ_m [34] governs the density of the massless Dirac operator $\not{D}$. The spectral density of Dirac operator is defined as [113]:

$$\rho(\lambda) = \lim_{V\to\infty} \frac{1}{V} \sum_k \langle \delta(\lambda - \lambda_k) \rangle \,, \tag{3.37}$$

where $i\lambda_k$ is the k-th eigenvalue of the $\not{D}$ with both volume V and gauge configuration fixed. Because the Euclidean Dirac operator cannot be guaranteed to be diagonalizable on the lattice, we measure the eigenvalues of the positive-definite operator $M = (\not{D} + m)^\dagger (\not{D} + m)$ (2.50) instead of measuring the eigenvalues of the Dirac operator directly. However, the computational complexity of finding the eigenvalues of M is expected to grow as $\mathcal{O}(V^k)$ where $k \geq 2$ and therefore, instead of the spectral density ρ, we access the scaling of the operator M by studying the mode number ν [159–161] that measures the number of eigenvalues of M smaller than Λ^2/V and is cheaper to calculate:

$$\nu(\Lambda) = 2 \int_0^{\sqrt{\Lambda^2 - m^2}} \rho(\lambda) \mathrm{d}\lambda \,. \tag{3.38}$$

On the lattice we could evaluate the eigenvalues of M directly using the algorithms described in [162], but instead we will use the stochastic implementation from [159], where the alternative formulation of the mode number is evaluated stochastically:

$$\nu(\Lambda) = \lim_{V\to\infty} \frac{1}{V} \left\langle \mathrm{tr}\ \mathbb{P}_\Lambda \right\rangle \,, \tag{3.39}$$

where $\mathbb{P}_\Lambda$ is an orthogonal projector to the eigenspace where eigenvalues have a maximum value of Λ^2. The projector $\mathbb{P}_\Lambda$ can be approximated with a rational ansatz:

$$\mathbb{P}_\Lambda \simeq h(\mathbb{X})^4 = \frac{1}{16} \left[1 - \mathbb{X} P(\mathbb{X}^2) \right]^4 \,, \qquad \mathbb{X} = 1 - \frac{2\Lambda_*^2}{M + \Lambda_*^2} \,, \tag{3.40}$$

where $h(x)$ approximates the step function $\theta(-x)$, P is a polynomial of degree n that minimizes the error function:

$$\delta = \max_{\varepsilon \leq x \leq 1} \left| 1 - \sqrt{x} P(x) \right| , \tag{3.41}$$

and Λ_* is a free parameter that can be chosen so that it minimizes the error caused by the approximation of step function with $h(x)$ in (3.40):

$$\frac{\Lambda}{\Lambda_*} = \left(\frac{1-\sqrt{\varepsilon}}{1+\sqrt{\varepsilon}}\right)^{1/2} + \int_{-\sqrt{\varepsilon}}^{\sqrt{\varepsilon}} dx \frac{1+x}{(1-x^2)^{3/2}} h(x)^4 \,. \tag{3.42}$$

The quality of the approximation can be estimated by checking how close Λ/Λ_* is to unity. We use $n = 32$, $\varepsilon = 0.01$, and tune P numerically to accuracy $\delta = 7.63 \times 10^{-4}$, which gives us the ratio $\Lambda/\Lambda_* \simeq 0.9624$.

The trace in (3.39) can be expensive to calculate directly and is instead evaluated stochastically [159]:

$$\langle \text{tr } \mathbb{P}_\Lambda \rangle \simeq \langle \mathcal{O}_N \rangle \,, \qquad \mathcal{O}_N = \frac{1}{N} \sum_{i=1}^{N} \eta_i^\dagger \mathbb{P}_\Lambda \eta_i \,, \tag{3.43}$$

where η_i are a new set of pseudofermion fields (2.51) satisfying an action:

$$S_\eta = \sum_{i=1}^{N} \eta_i^\dagger \eta_i \,. \tag{3.44}$$

These Gaussian noise vectors are generated separately for each gauge field configuration during the simulation. The accuracy of measuring the expectation value $\langle \mathcal{O}_N \rangle$ instead of $\langle \text{tr } \mathbb{P}_\Lambda \rangle$ is given by:

$$\left\langle \left(\mathcal{O}_N - \langle \mathcal{O}_N \rangle\right)^2 \right\rangle = \left\langle \left(\text{tr } \mathbb{P}_\Lambda - \langle \text{tr } \mathbb{P}_\Lambda \rangle\right)^2 \right\rangle + \frac{1}{N} \nu(\Lambda) \,, \tag{3.45}$$

i.e. the accuracy increases as more pseudofermion fields η_i are added. In practice we have found the choice $N = 3$ to be sufficient.

At the IRFP the mode number scales as a power law [160]:

$$\nu(\Lambda) \simeq \nu_0(m) + C \left[\Lambda^2 - m^2\right]^{\frac{2}{1+\gamma_m^*}} \simeq C \Lambda^{\frac{4}{1+\gamma_m^*}} \,, \tag{3.46}$$

where on the second equality, we have assumed the mass dependent terms to be small, since the model is massless. The range of Λ where this power law holds, has to be tuned manually. In figure 3.15 we show the fit of our data to (3.46) and the fit range used to determine γ_m^* for the largest lattice sizes used. The curves are shown in the order of descending coupling. The step-like structure in the small Λ region is caused by the lowest eigenvalues being discrete. The effect is more prominent at small couplings, while at large couplings the curve is smoother due to interactions. This method is sensitive to the lattice size, as with the smaller lattices the range where a stable fit can be made becomes narrow due

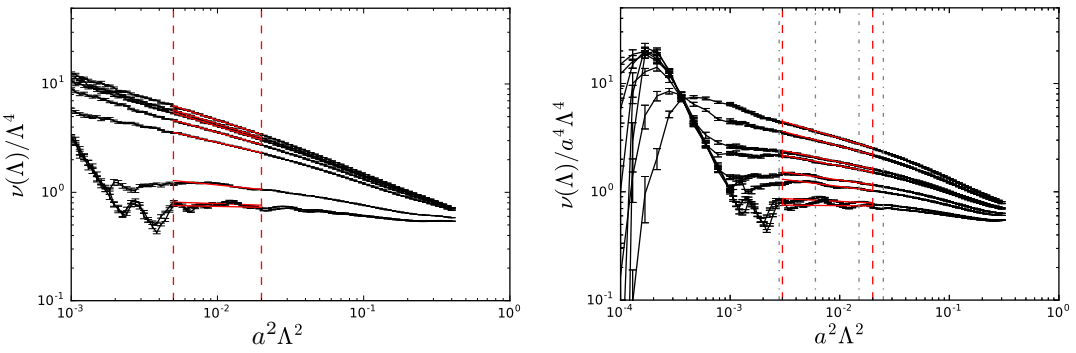

Figure 3.15: The mode number divided by $a^4\Lambda^4$ as a function of $a^2\Lambda^2$ for: *Left:* $N_f = 6$ and *Right:* $N_f = 8$. The dashed lines indicate the chosen fit range.

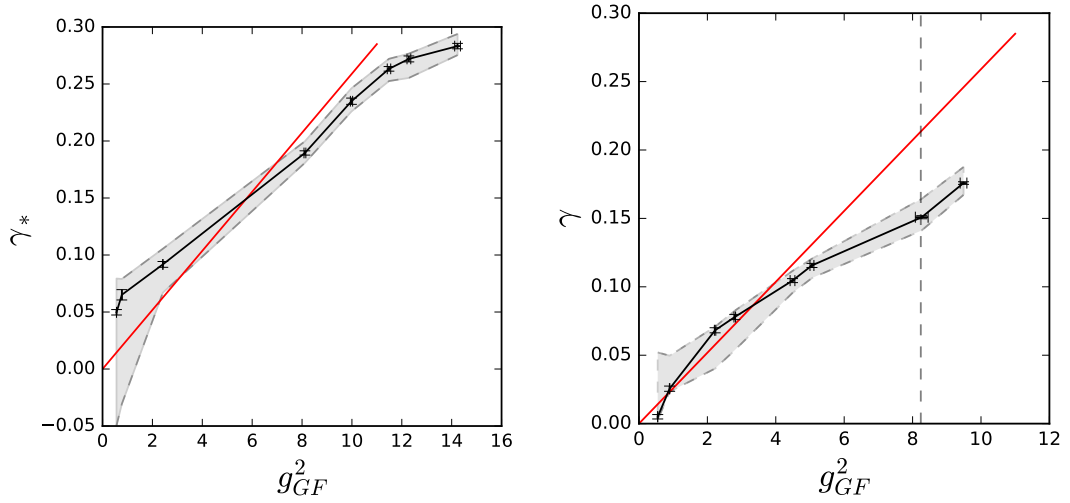

Figure 3.16: he mass anomalous dimension γ_m^* using the spectral density method (3.38) for *Left:* $N_f = 6$ and *Right:* $N_f = 8$. The shaded bands illustrates the uncertainty from varying the fit range by 50%.

to an increase in both infrared finite size effects and ultraviolet lattice spacing effects. Because of this we do not try a continuum extrapolation with this method.

After a power law fit to the mode number data, we show the γ_m^* measurement in figure 3.16. The figure has two sets of errors, the errors on the points are statistical error measured with the Jackknife method, and the shaded bands are the errors from changing the fit region. As noted before, the eigenvalues are more discrete at the smaller couplings, which is seen in the figure as a increased errors. However, compared to the step scaling method, the spectral density gives stable results at high couplings near the IRFP. We measure $\gamma_m^* = 0.283(2)^{+0.01}_{-0.01}$ for $N_f = 6$ [2] and $\gamma_m^* = 0.15^{+0.02}_{-0.02}$ for $N_f = 8$ [1]. While no numbers for the step scaling result are reported, we see figures 3.14 and 3.16 giving compatible results.

Chapter 4

Summary

The determination of the vacuum phase structure in non-Abelian gauge theories with multiple fermions is an ongoing endeavor of the lattice community that could benefit the model building in beyond the Standard Model scenarios. In this thesis, we have studied the infrared behavior of the SU(2) gauge model with six and eight massless Dirac fermions transforming in the fundamental representation. These models were chosen due to different perturbative estimates predicting them to be around the lower boundary of the conformal window. However, the infrared fixed point appears at large coupling and perturbative estimates are not expected to hold true. Therefore, non-perturbative methods are needed.The previous lattice studies on these models have been inconclusive.

We have done extensive simulations in both of the models and confirmed the existence of the infrared fixed point in both the six and eight fermion theories. In our chosen scheme we observed the IRFP at $g^2_{\rm GF} = 14.5(4)^{+0.4}_{-1.2}$ for the $N_f = 6$ theory, and $g^2_{\rm GF} = 8.24(59)^{+0.97}_{-1.64}$ for the $N_f = 8$ theory. The results remain robust with the change of scheme parameter c_t, discretization choices and analysis parameters. After the completion of this thesis, a subsequent study on the mass spectrum of SU(2) gauge theory was released [163], which further strengthens the existence of IRFP in the $N_f = 6$ theory.

After confirming the existence of the IRFP, we measured two scheme irrelevant quantities at the IRFP. The mass anomalous dimension γ^*_m was measured using two different methods: the mass step scaling and the spectral density method. We observe the step scaling method to become unstable at large coupling. On the other hand, the spectral density method gives a stable result and we get $\gamma^*_m = 0.283(2)^{+0.01}_{-0.01}$ for the $N_f = 6$ theory, and $\gamma^*_m = 0.15^{+0.02}_{-0.02}$ for the $N_f = 8$ theory. However, it should be noted that these γ^*_m are measured at a fixed lattice size and a proper continuum limit is still lacking.

The leading irrelevant exponent of the coupling γ_g^* was measured from the slope of the β-function to be $\gamma_g^* = 0.648(97)^{+0.16}_{-0.1}$ for the $N_f = 6$ theory, and $\gamma_g^* = 0.66(4)^{+0.25}_{-0.13}$ for the $N_f = 8$ theory. These values are close to the scheme independent perturbative estimate of $\gamma_g^* = 0.6515$ for the $N_f = 6$ theory, and $\gamma_g^* = 0.25$ for the $N_f = 8$ theory. Again, the measurement of γ_g^* remained robust under the change of parameters.

Since the four fermion model is known to be chirally broken, we can deduce that the lower edge of the conformal window must lie between four and six fermions. The five fermions model could still be walking, but lattice simulations with odd number of fermions are more expensive. One interesting concept we will look into in the future, is adding masses to some or all the six fermions to see how the theory breaks out of the conformal symmetry, because the masses explicitly break the conformal symmetry. Similar ideas have been studied for the SU(3) model in [164]. Another interesting topic for future study, would be a SU(2) model with large number of fermions, since some theoretical results indicate that there could be an non-trivial UV fixed point in theories with number of fermions above the $N_f^{\max} = 11$ [165].

Bibliography

[4] **ATLAS** Collaboration, G. Aad et al., *Observation of a new particle in the search for the Standard Model Higgs boson with the ATLAS detector at the LHC*, *Phys. Lett.* **B716** (2012) 1–29, [arXiv:1207.7214].

[5] **CMS** Collaboration, S. Chatrchyan et al., *Observation of a new boson at a mass of 125 GeV with the CMS experiment at the LHC*, *Phys. Lett.* **B716** (2012) 30–61, [arXiv:1207.7235].

[6] **Particle Data Group** Collaboration, C. Patrignani et al., *Review of Particle Physics*, *Chin. Phys.* **C40** (2016), no. 10 100001.

[7] M. Gell-Mann, *A schematic model of baryons and mesons*, *Phys. Letters* **8** (1964) 214.

[8] G. Zweig, *An su(3) model for strong interaction symmetry and its breaking*, tech. rep., CM-P00042884, 1964.

[9] O. W. Greenberg, *Spin and unitary-spin independence in a paraquark model of baryons and mesons*, *Physical Review Letters* **13** (1964), no. 20 598.

[10] Y. Nambu, *A systematics of hadrons*, *Subnuclear physics.* (1966) 133–142.

[11] M.-Y. Han and Y. Nambu, *Three-triplet model with double su (3) symmetry*, *Physical Review* **139** (1965), no. 4B B1006.

[12] S. Weinberg, *A Model of Leptons*, *Phys. Rev. Lett.* **19** (1967) 1264–1266.

[13] P. W. Higgs, *Broken Symmetries and the Masses of Gauge Bosons*, *Phys. Rev. Lett.* **13** (1964) 508–509.

[14] F. Englert and R. Brout, *Broken Symmetry and the Mass of Gauge Vector Mesons*, *Phys. Rev. Lett.* **13** (1964) 321–323.

[15] J. Goldstone, *Field theories with «superconductor» solutions*, *Il Nuovo Cimento (1955-1965)* **19** (1961), no. 1 154–164.

[16] M. Gell-Mann, *The Symmetry group of vector and axial vector currents*, *Physics* **1** (1964) 63–75.

[17] G. 't Hooft and M. J. G. Veltman, *Regularization and Renormalization of Gauge Fields*, *Nucl. Phys.* **B44** (1972) 189–213.

[18] C. G. Callan, Jr., *Broken scale invariance in scalar field theory*, *Phys. Rev.* **D2** (1970) 1541–1547.

[19] K. Symanzik, *Small distance behavior in field theory and power counting*, *Commun. Math. Phys.* **18** (1970) 227–246.

[20] D. J. Gross, *Applications of the Renormalization Group to High-Energy Physics*, pp. 141–250. North-Holland Publishing CO., 1976.

[21] H. D. Politzer, *Reliable Perturbative Results for Strong Interactions?*, *Phys. Rev. Lett.* **30** (1973) 1346–1349.

[22] W. E. Caswell, *Asymptotic Behavior of Nonabelian Gauge Theories to Two Loop Order*, *Phys. Rev. Lett.* **33** (1974) 244.

[23] D. R. T. Jones, *Two Loop Diagrams in Yang-Mills Theory*, *Nucl. Phys.* **B75** (1974) 531.

[24] O. V. Tarasov, A. A. Vladimirov, and A. Yu. Zharkov, *The Gell-Mann-Low Function of QCD in the Three Loop Approximation*, *Phys. Lett.* **93B** (1980) 429–432.

[25] T. van Ritbergen, J. A. M. Vermaseren, and S. A. Larin, *The Four loop beta function in quantum chromodynamics*, *Phys. Lett.* **B400** (1997) 379–384, [hep-ph/9701390].

[26] T. Luthe, A. Maier, P. Marquard, and Y. Schröder, *Towards the five-loop Beta function for a general gauge group*, *JHEP* **07** (2016) 127, [arXiv:1606.08662].

[27] P. A. Baikov, K. G. Chetyrkin, and J. H. Kühn, *Five-Loop Running of the QCD coupling constant*, *Phys. Rev. Lett.* **118** (2017), no. 8 082002, [arXiv:1606.08659].

[28] F. Herzog, B. Ruijl, T. Ueda, J. A. M. Vermaseren, and A. Vogt, *The five-loop beta function of Yang-Mills theory with fermions*, *JHEP* **02** (2017) 090, [arXiv:1701.01404].

[29] W. A. Bardeen, A. J. Buras, D. W. Duke, and T. Muta, *Deep Inelastic Scattering Beyond the Leading Order in Asymptotically Free Gauge Theories*, *Phys. Rev.* **D18** (1978) 3998.

[30] J. A. M. Vermaseren, S. A. Larin, and T. van Ritbergen, *The four loop quark mass anomalous dimension and the invariant quark mass*, *Phys. Lett.* **B405** (1997) 327–333, [hep-ph/9703284].

[31] P. A. Baikov, K. G. Chetyrkin, and J. H. Kühn, *Quark Mass and Field Anomalous Dimensions to $\mathcal{O}(\alpha_s^5)$*, *JHEP* **10** (2014) 076, [arXiv:1402.6611].

[32] T. Luthe, A. Maier, P. Marquard, and Y. Schröder, *Five-loop quark mass and field anomalous dimensions for a general gauge group*, *JHEP* **01** (2017) 081, [arXiv:1612.05512].

[33] P. A. Baikov, K. G. Chetyrkin, and J. H. Kühn, *Five-loop fermion anomalous dimension for a general gauge group from four-loop massless propagators*, *JHEP* **04** (2017) 119, [arXiv:1702.01458].

[34] L. Del Debbio and R. Zwicky, *Hyperscaling relations in mass-deformed conformal gauge theories*, *Phys. Rev.* **D82** (2010) 014502, [arXiv:1005.2371].

[35] L. Del Debbio and R. Zwicky, *Scaling relations for the entire spectrum in mass-deformed conformal gauge theories*, *Phys. Lett.* **B700** (2011) 217–220, [arXiv:1009.2894].

[36] T. Banks and A. Zaks, *On the Phase Structure of Vector-Like Gauge Theories with Massless Fermions*, *Nucl. Phys.* **B196** (1982) 189.

[37] T. Appelquist, K. D. Lane, and U. Mahanta, *On the Ladder Approximation for Spontaneous Chiral Symmetry Breaking*, *Phys. Rev. Lett.* **61** (1988) 1553.

[38] A. G. Cohen and H. Georgi, *Walking Beyond the Rainbow*, *Nucl. Phys.* **B314** (1989) 7–24.

[39] F. Sannino and K. Tuominen, *Orientifold theory dynamics and symmetry breaking*, *Phys. Rev.* **D71** (2005) 051901, [hep-ph/0405209].

[40] D. D. Dietrich and F. Sannino, *Conformal window of SU(N) gauge theories with fermions in higher dimensional representations*, *Phys. Rev.* **D75** (2007) 085018, [hep-ph/0611341].

[41] T. Appelquist, A. G. Cohen, and M. Schmaltz, *A New constraint on strongly coupled gauge theories*, *Phys. Rev.* **D60** (1999) 045003, [hep-th/9901109].

[42] T. A. Ryttov and F. Sannino, *Supersymmetry inspired QCD beta function*, *Phys. Rev.* **D78** (2008) 065001, [arXiv:0711.3745].

[43] O. Antipin and K. Tuominen, *Resizing the Conformal Window: A beta function Ansatz*, *Phys. Rev.* **D81** (2010) 076011, [arXiv:0909.4879].

[44] C. Pica and F. Sannino, *Beta Function and Anomalous Dimensions*, *Phys. Rev.* **D83** (2011) 116001, [arXiv:1011.3832].

[45] M. T. Frandsen, T. Pickup, and M. Teper, *Delineating the conformal window*, *Phys. Lett.* **B695** (2011) 231–237, [arXiv:1007.1614].

[46] H. Georgi, *Unparticle physics*, *Phys. Rev. Lett.* **98** (2007) 221601, [hep-ph/0703260].

[47] H. Georgi, *Another odd thing about unparticle physics*, *Phys. Lett.* **B650** (2007) 275–278, [arXiv:0704.2457].

[48] S. Weinberg, *Implications of Dynamical Symmetry Breaking: An Addendum*, *Phys. Rev.* **D19** (1979) 1277–1280.

[49] L. Susskind, *Dynamics of Spontaneous Symmetry Breaking in the Weinberg-Salam Theory*, *Phys. Rev.* **D20** (1979) 2619–2625.

[50] E. Eichten and K. D. Lane, *Dynamical Breaking of Weak Interaction Symmetries*, *Phys. Lett.* **B90** (1980) 125–130.

[51] S. Dimopoulos and L. Susskind, *Mass without scalars*, *Nuclear Physics B* **155** (1979), no. 1 237–252.

[52] R. P. Feynman, *Space-time approach to nonrelativistic quantum mechanics*, *Rev. Mod. Phys.* **20** (1948) 367–387.

[53] H. J. Rothe, *Lattice Gauge Theories: An Introduction Third Edition*, vol. 74. World Scientific Publishing Company, 2005.

[54] N. Metropolis, A. W. Rosenbluth, M. N. Rosenbluth, A. H. Teller, and E. Teller, *Equation of state calculations by fast computing machines*, *The journal of chemical physics* **21** (1953), no. 6 1087–1092.

[55] W. K. Hastings, *Monte carlo sampling methods using markov chains and their applications*, *Biometrika* **57** (1970), no. 1 97–109.

[56] J.-S. Wang, *Cluster monte carlo algorithms and their applications*, in *Asian Conference on Computer Vision*, pp. 307–315, Springer, 1995.

[57] S. Duane, A. D. Kennedy, B. J. Pendleton, and D. Roweth, *Hybrid Monte Carlo*, *Phys. Lett.* **B195** (1987) 216–222.

[58] I. Omelyan, I. Mryglod, and R. Folk, *Construction of high-order force-gradient algorithms for integration of motion in classical and quantum systems*, *Physical Review E* **66** (2002), no. 2 026701.

[59] I. P. Omelyan, I. M. Mryglod, and R. Folk, *Symplectic analytically integrable decomposition algorithms: classification, derivation, and application to molecular dynamics, quantum and celestial mechanics simulations*, *Computer Physics Communications* **151** (2003), no. 3 272–314.

[60] T. Takaishi and P. de Forcrand, *Testing and tuning new symplectic integrators for hybrid Monte Carlo algorithm in lattice QCD*, *Phys. Rev.* **E73** (2006) 036706, [hep-lat/0505020].

[61] K. G. Wilson, *Confinement of Quarks*, *Phys. Rev.* **D10** (1974) 2445–2459. [,45(1974)].

[62] L. Susskind, *Lattice Fermions*, *Phys. Rev.* **D16** (1977) 3031–3039.

[63] H. S. Sharatchandra, H. J. Thun, and P. Weisz, *Susskind Fermions on a Euclidean Lattice*, *Nucl. Phys.* **B192** (1981) 205–236.

[64] K. Jansen, *Domain wall fermions and chiral gauge theories*, *Phys. Rept.* **273** (1996) 1–54, [hep-lat/9410018].

[65] H. Neuberger, *Exactly massless quarks on the lattice*, *Phys. Lett.* **B417** (1998) 141–144, [hep-lat/9707022].

[66] H. B. Nielsen and M. Ninomiya, *No Go Theorem for Regularizing Chiral Fermions*, *Phys. Lett.* **105B** (1981) 219–223.

[67] K. Symanzik, *Some Topics in Quantum Field Theory*, in *Mathematical problems in theoretical physics. Proceedings, 6th International Conference on Mathematical Physics, West Berlin, Germany, 11-20.8, 1981*, pp. 47–58, 1981.

[68] K. Symanzik, *Continuum Limit and Improved Action in Lattice Theories. 1. Principles and phi**4 Theory*, *Nucl. Phys.* **B226** (1983) 187–204.

[69] K. Symanzik, *Continuum Limit and Improved Action in Lattice Theories. 2. O(N) Nonlinear Sigma Model in Perturbation Theory*, *Nucl. Phys.* **B226** (1983) 205–227.

[70] M. Luscher, S. Sint, R. Sommer, and P. Weisz, *Chiral symmetry and O(a) improvement in lattice QCD*, *Nucl. Phys.* **B478** (1996) 365–400, [hep-lat/9605038].

[71] M. Luscher and P. Weisz, *On-Shell Improved Lattice Gauge Theories*, *Commun. Math. Phys.* **97** (1985) 59. [Erratum: Commun. Math. Phys.98,433(1985)].

[72] B. Sheikholeslami and R. Wohlert, *Improved Continuum Limit Lattice Action for QCD with Wilson Fermions*, *Nucl. Phys.* **B259** (1985) 572.

[73] M. Luscher, S. Sint, R. Sommer, and H. Wittig, *Nonperturbative determination of the axial current normalization constant in O(a) improved lattice QCD*, *Nucl. Phys.* **B491** (1997) 344–364, [hep-lat/9611015].

[74] R. Wohlert, *Improved Continuum Limit Lattice Action for Quarks*, .

[75] T. DeGrand, Y. Shamir, and B. Svetitsky, *Infrared fixed point in SU(2) gauge theory with adjoint fermions*, *Phys. Rev.* **D83** (2011) 074507, [arXiv:1102.2843].

[76] S. Capitani, S. Durr, and C. Hoelbling, *Rationale for UV-filtered clover fermions*, *JHEP* **11** (2006) 028, [hep-lat/0607006].

[77] Y. Shamir, B. Svetitsky, and E. Yurkovsky, *Improvement via hypercubic smearing in triplet and sextet QCD*, *Phys. Rev.* **D83** (2011) 097502, [arXiv:1012.2819].

[78] **QCDSF** Collaboration, R. Horsley, H. Perlt, P. E. L. Rakow, G. Schierholz, and A. Schiller, *One-loop renormalisation of quark bilinears for overlap fermions with improved gauge actions*, *Nucl. Phys.* **B693** (2004) 3–35, [hep-lat/0404007]. [Erratum: Nucl. Phys.B713,601(2005)].

[79] Y. Iwasaki, *Renormalization Group Analysis of Lattice Theories and Improved Lattice Action. II. Four-dimensional non-Abelian SU(N) gauge model*, arXiv:1111.7054.

[80] M. Luscher, R. Narayanan, P. Weisz, and U. Wolff, *The Schrödinger functional: A Renormalizable probe for nonAbelian gauge theories*, *Nucl. Phys.* **B384** (1992) 168–228, [hep-lat/9207009].

[81] M. Luscher and P. Weisz, *O(a) improvement of the axial current in lattice QCD to one loop order of perturbation theory*, *Nucl. Phys.* **B479** (1996) 429–458, [hep-lat/9606016].

[82] R. Sommer, *Non-perturbative QCD: Renormalization, O(a)-improvement and matching to Heavy Quark Effective Theory*, in *Workshop on Perspectives in Lattice QCD Nara, Japan, October 31-November 11, 2005*, 2006. hep-lat/0611020.

[83] S. Aoki, R. Frezzotti, and P. Weisz, *Computation of the improvement coefficient c(SW) to one loop with improved gluon actions*, *Nucl. Phys.* **B540** (1999) 501–519, [hep-lat/9808007].

[84] J. Bulava and S. Schaefer, *Improvement of $N_f = 3$ lattice QCD with Wilson fermions and tree-level improved gauge action*, *Nucl. Phys.* **B874** (2013) 188–197, [arXiv:1304.7093].

[85] S. Sint, *On the Schrodinger functional in QCD*, *Nucl. Phys.* **B421** (1994) 135–158, [hep-lat/9312079].

[86] **ALPHA** Collaboration, S. Capitani, M. Luscher, R. Sommer, and H. Wittig, *Nonperturbative quark mass renormalization in quenched lattice QCD*, *Nucl. Phys.* **B544** (1999) 669–698, [hep-lat/9810063].

[87] **ALPHA** Collaboration, S. Sint and P. Weisz, *The Running quark mass in the SF scheme and its two loop anomalous dimension*, *Nucl. Phys.* **B545** (1999) 529–542, [hep-lat/9808013].

[88] K. Jansen, C. Liu, M. Luscher, H. Simma, S. Sint, R. Sommer, P. Weisz, and U. Wolff, *Nonperturbative renormalization of lattice QCD at all scales*, *Phys. Lett.* **B372** (1996) 275–282, [hep-lat/9512009].

[89] D. H. Weingarten and D. N. Petcher, *Monte Carlo Integration for Lattice Gauge Theories with Fermions*, *Phys. Lett.* **99B** (1981) 333–338.

[90] M. Hestenes and E. Stiefel, *Methods of conjugate gradients for solving linear systems*, *Journal of research of the National Bureau of Standards* **49** (1952), no. 6 409–436.

[91] T. A. DeGrand and P. Rossi, *Conditioning Techniques for Dynamical Fermions*, *Comput. Phys. Commun.* **60** (1990) 211–214.

[92] J. A. Meijerink and H. A. van der Vorst, *An iterative solution method for linear systems of which the coefficient matrix is a symmetric $\mathcal{M}$-matrix*, *Mathematics of computation* **31** (1977), no. 137 148–162.

[93] Y. Oyanagi, *An incomplete ldu decomposition of lattice fermions and its application to conjugate residual methods*, *Computer physics communications* **42** (1986), no. 3 333–343.

[94] M. Hasenbusch, *Speeding up the hybrid Monte Carlo algorithm for dynamical fermions*, *Phys. Lett.* **B519** (2001) 177–182, [hep-lat/0107019].

[95] M. Hasenbusch and K. Jansen, *Speeding up lattice QCD simulations with clover improved Wilson fermions*, *Nucl. Phys.* **B659** (2003) 299–320, [hep-lat/0211042].

[96] C. Urbach, K. Jansen, A. Shindler, and U. Wenger, *HMC algorithm with multiple time scale integration and mass preconditioning*, *Comput. Phys. Commun.* **174** (2006) 87–98, [hep-lat/0506011].

[97] T. DeGrand, Y. Shamir, and B. Svetitsky, *Running coupling and mass anomalous dimension of SU(3) gauge theory with two flavors of symmetric-representation fermions*, *Phys. Rev.* **D82** (2010) 054503, [arXiv:1006.0707].

[98] C. Morningstar and M. J. Peardon, *Analytic smearing of SU(3) link variables in lattice QCD*, *Phys. Rev.* **D69** (2004) 054501, [hep-lat/0311018].

[99] A. Hasenfratz and F. Knechtli, *Flavor symmetry and the static potential with hypercubic blocking*, *Phys. Rev.* **D64** (2001) 034504, [hep-lat/0103029].

[100] J. Rantaharju, T. Rantalaiho, K. Rummukainen, and K. Tuominen, *Running coupling in SU(2) gauge theory with two adjoint fermions*, *Phys. Rev.* **D93** (2016), no. 9 094509, [arXiv:1510.03335].

[101] E. T. Neil, *Exploring Models for New Physics on the Lattice*, *PoS* **LATTICE2011** (2011) 009, [arXiv:1205.4706].

[102] C. Pica, *Beyond the Standard Model: Charting Fundamental Interactions via Lattice Simulations*, *PoS* **LATTICE2016** (2016) 015, [arXiv:1701.07782].

[103] B. Svetitsky, *Looking behind the Standard Model with lattice gauge theory*, in *35th International Symposium on Lattice Field Theory (Lattice 2017) Granada, Spain, June 18-24, 2017*, 2017. arXiv:1708.04840.

[104] A. J. Hietanen, J. Rantaharju, K. Rummukainen, and K. Tuominen, *Spectrum of SU(2) lattice gauge theory with two adjoint Dirac flavours*, *JHEP* **05** (2009) 025, [arXiv:0812.1467].

[105] A. J. Hietanen, K. Rummukainen, and K. Tuominen, *Evolution of the coupling constant in SU(2) lattice gauge theory with two adjoint fermions*, *Phys. Rev.* **D80** (2009) 094504, [arXiv:0904.0864].

[106] L. Del Debbio, A. Patella, and C. Pica, *Higher representations on the lattice: Numerical simulations. SU(2) with adjoint fermions*, *Phys. Rev.* **D81** (2010) 094503, [arXiv:0805.2058].

[107] S. Catterall, J. Giedt, F. Sannino, and J. Schneible, *Phase diagram of SU(2) with 2 flavors of dynamical adjoint quarks*, *JHEP* **11** (2008) 009, [arXiv:0807.0792].

[108] F. Bursa, L. Del Debbio, L. Keegan, C. Pica, and T. Pickup, *Mass anomalous dimension in SU(2) with two adjoint fermions*, *Phys. Rev.* **D81** (2010) 014505, [arXiv:0910.4535].

[109] L. Del Debbio, B. Lucini, A. Patella, C. Pica, and A. Rago, *Conformal versus confining scenario in SU(2) with adjoint fermions*, *Phys. Rev.* **D80** (2009) 074507, [arXiv:0907.3896].

[110] L. Del Debbio, B. Lucini, A. Patella, C. Pica, and A. Rago, *The infrared dynamics of Minimal Walking Technicolor*, *Phys. Rev.* **D82** (2010) 014510, [arXiv:1004.3206].

[111] L. Del Debbio, B. Lucini, A. Patella, C. Pica, and A. Rago, *Mesonic spectroscopy of Minimal Walking Technicolor*, *Phys. Rev.* **D82** (2010) 014509, [arXiv:1004.3197].

[112] F. Bursa, L. Del Debbio, D. Henty, E. Kerrane, B. Lucini, A. Patella, C. Pica, T. Pickup, and A. Rago, *Improved Lattice Spectroscopy of Minimal Walking Technicolor*, *Phys. Rev.* **D84** (2011) 034506, [arXiv:1104.4301].

[113] A. Patella, *A precise determination of the psibar-psi anomalous dimension in conformal gauge theories*, *Phys. Rev.* **D86** (2012) 025006, [arXiv:1204.4432].

[114] J. Giedt and E. Weinberg, *Finite size scaling in minimal walking technicolor*, *Phys. Rev.* **D85** (2012) 097503, [arXiv:1201.6262].

[115] L. Del Debbio, B. Lucini, A. Patella, C. Pica, and A. Rago, *Large volumes and spectroscopy of walking theories*, *Phys. Rev.* **D93** (2016), no. 5 054505, [arXiv:1512.08242].

[116] J. Rantaharju, *Gradient Flow Coupling in the SU(2) gauge theory with two adjoint fermions*, *Phys. Rev.* **D93** (2016), no. 9 094516, [arXiv:1512.02793].

[117] A. Hietanen, R. Lewis, C. Pica, and F. Sannino, *Fundamental Composite Higgs Dynamics on the Lattice: SU(2) with Two Flavors*, *JHEP* **07** (2014) 116, [arXiv:1404.2794].

[118] R. Lewis, C. Pica, and F. Sannino, *Light Asymmetric Dark Matter on the Lattice: SU(2) Technicolor with Two Fundamental Flavors*, *Phys. Rev.* **D85** (2012) 014504, [arXiv:1109.3513].

[119] T. Karavirta, J. Rantaharju, K. Rummukainen, and K. Tuominen, *Determining the conformal window: SU(2) gauge theory with $N_f = 4$, 6 and 10 fermion flavours*, *JHEP* **05** (2012) 003, [arXiv:1111.4104].

[120] F. Bursa, L. Del Debbio, L. Keegan, C. Pica, and T. Pickup, *Mass anomalous dimension in SU(2) with six fundamental fermions*, *Phys. Lett.* **B696** (2011) 374–379, [arXiv:1007.3067].

[121] M. Hayakawa, K. I. Ishikawa, S. Takeda, and N. Yamada, *Running coupling constant and mass anomalous dimension of six-flavor SU(2) gauge theory*, *Phys. Rev.* **D88** (2013), no. 9 094504, [arXiv:1307.6997].

[122] T. Appelquist, R. Brower, M. Buchoff, M. Cheng, G. Fleming, J. Kiskis, M. Lin, E. Neil, J. Osborn, C. Rebbi, et al., *Two-Color Gauge Theory with Novel Infrared Behavior*, *Phys. Rev. Lett.* **112** (2014), no. 11 111601, [arXiv:1311.4889].

[123] H. Ohki, T. Aoyama, E. Itou, M. Kurachi, C. J. D. Lin, H. Matsufuru, T. Onogi, E. Shintani, and T. Yamazaki, *Study of the scaling properties in*

SU(2) gauge theory with eight flavors, *PoS* **LATTICE2010** (2010) 066, [arXiv:1011.0373].

[124] R. Narayanan and H. Neuberger, *Infinite N phase transitions in continuum Wilson loop operators*, *JHEP* **03** (2006) 064, [hep-th/0601210].

[125] M. Luscher, *Trivializing maps, the Wilson flow and the HMC algorithm*, *Commun. Math. Phys.* **293** (2010) 899–919, [arXiv:0907.5491].

[126] M. Lüscher, *Properties and uses of the Wilson flow in lattice QCD*, *JHEP* **08** (2010) 071, [arXiv:1006.4518]. [Erratum: JHEP03,092(2014)].

[127] A. Ramos, *The Yang-Mills gradient flow and renormalization*, *PoS* **LATTICE2014** (2015) 017, [arXiv:1506.00118].

[128] P. Fritzsch, M. Dalla Brida, T. Korzec, A. Ramos, S. Sint, and R. Sommer, *Towards a new determination of the QCD Lambda parameter from running couplings in the three-flavour theory*, *PoS* **LATTICE2014** (2014) 291, [arXiv:1411.7648].

[129] J. Rantaharju, *The Gradient Flow Coupling in Minimal Walking Technicolor*, *PoS* **Lattice2013** (2014) 084, [arXiv:1311.3719].

[130] R. Sommer, *Scale setting in lattice QCD*, *PoS* **LATTICE2013** (2014) 015, [arXiv:1401.3270].

[131] C. Alexandrou, A. Athenodorou, K. Cichy, A. Dromard, E. Garcia-Ramos, K. Jansen, U. Wenger, and F. Zimmermann, *Comparison of topological charge definitions in Lattice QCD*, arXiv:1708.00696.

[132] M. Kitazawa, M. Asakawa, T. Hatsuda, T. Iritani, E. Itou, and H. Suzuki, *Measurement of thermodynamics using gradient flow*, *PoS* **LATTICE2014** (2014) 022, [arXiv:1412.4508].

[133] M. Luscher and P. Weisz, *Perturbative analysis of the gradient flow in non-abelian gauge theories*, *JHEP* **02** (2011) 051, [arXiv:1101.0963].

[134] M. Luscher, *Chiral symmetry and the Yang–Mills gradient flow*, *JHEP* **04** (2013) 123, [arXiv:1302.5246].

[135] R. V. Harlander and T. Neumann, *The perturbative QCD gradient flow to three loops*, *JHEP* **06** (2016) 161, [arXiv:1606.03756].

[136] Z. Fodor, K. Holland, J. Kuti, D. Nogradi, and C. H. Wong, *The Yang-Mills gradient flow in finite volume*, *JHEP* **11** (2012) 007, [arXiv:1208.1051].

[137] Z. Fodor, K. Holland, J. Kuti, D. Nogradi, and C. H. Wong, *The gradient flow running coupling scheme*, *PoS* **LATTICE2012** (2012) 050, [arXiv:1211.3247].

[138] Z. Fodor, K. Holland, J. Kuti, S. Mondal, D. Nogradi, and C. H. Wong, *The lattice gradient flow at tree-level and its improvement*, *JHEP* **09** (2014) 018, [arXiv:1406.0827].

[139] A. Ramos, *The gradient flow running coupling with twisted boundary conditions*, *JHEP* **11** (2014) 101, [arXiv:1409.1445].

[140] P. Fritzsch and A. Ramos, *The gradient flow coupling in the Schrödinger Functional*, *JHEP* **10** (2013) 008, [arXiv:1301.4388].

[141] M. Lüscher, *Step scaling and the Yang-Mills gradient flow*, *JHEP* **06** (2014) 105, [arXiv:1404.5930].

[142] A. Rubeo and S. Sint, *Perturbative $O(a^2)$ effects in gradient flow couplings with SF and SF-open boundary conditions*, *PoS* **LATTICE2016** (2016) 388, [arXiv:1612.07047].

[143] C. J. D. Lin, K. Ogawa, and A. Ramos, *The Yang-Mills gradient flow and SU(3) gauge theory with 12 massless fundamental fermions in a colour-twisted box*, *JHEP* **12** (2015) 103, [arXiv:1510.05755].

[144] A. Ramos and S. Sint, *Symanzik improvement of the gradient flow in lattice gauge theories*, *Eur. Phys. J.* **C76** (2016), no. 1 15, [arXiv:1508.05552].

[145] **ALPHA** Collaboration, M. Dalla Brida, P. Fritzsch, T. Korzec, A. Ramos, S. Sint, and R. Sommer, *Slow running of the Gradient Flow coupling from 200 MeV to 4 GeV in $N_{\rm f} = 3$ QCD*, *Phys. Rev.* **D95** (2017), no. 1 014507, [arXiv:1607.06423].

[146] N. Kamata and S. Sasaki, *Numerical study of tree-level improved lattice gradient flows in pure Yang-Mills theory*, *Phys. Rev.* **D95** (2017), no. 5 054501, [arXiv:1609.07115].

[147] A. Cheng, A. Hasenfratz, Y. Liu, G. Petropoulos, and D. Schaich, *Improving the continuum limit of gradient flow step scaling*, *JHEP* **05** (2014) 137, [arXiv:1404.0984].

[148] L. Del Debbio, H. Panagopoulos, and E. Vicari, *theta dependence of SU(N) gauge theories*, *JHEP* **08** (2002) 044, [hep-th/0204125].

[149] **ALPHA** Collaboration, S. Schaefer, R. Sommer, and F. Virotta, *Critical slowing down and error analysis in lattice QCD simulations*, *Nucl. Phys.* **B845** (2011) 93–119, [arXiv:1009.5228].

[150] P. Fritzsch, A. Ramos, and F. Stollenwerk, *Critical slowing down and the gradient flow coupling in the Schrödinger functional*, *PoS* **Lattice2013** (2014) 461, [arXiv:1311.7304].

[151] T. Karavirta, A. Mykkanen, J. Rantaharju, K. Rummukainen, and K. Tuominen, *Nonperturbative improvement of SU(2) lattice gauge theory with adjoint or fundamental flavors*, *JHEP* **06** (2011) 061, [arXiv:1101.0154].

[152] A. Hasenfratz and D. Schaich, *Nonperturbative β function of twelve-flavor SU(3) gauge theory*, *JHEP* **02** (2018) 132, [arXiv:1610.10004].

[153] M. Luscher, R. Sommer, P. Weisz, and U. Wolff, *A Precise determination of the running coupling in the SU(3) Yang-Mills theory*, *Nucl. Phys.* **B413** (1994) 481–502, [hep-lat/9309005].

[154] T. A. Ryttov and R. Shrock, *Higher-order scheme-independent series expansions of $\gamma_{\bar{\psi}\psi,IR}$ and β'_{IR} in conformal field theories*, *Phys. Rev.* **D95** (2017), no. 10 105004, [arXiv:1703.08558].

[155] T. A. Ryttov and R. Shrock, *Higher-Order Scheme-Independent Calculations of Physical Quantities in the Conformal Phase of a Gauge Theory*, *Phys. Rev.* **D95** (2017), no. 8 085012, [arXiv:1701.06083].

[156] T. Appelquist, G. T. Fleming, and E. T. Neil, *Lattice Study of Conformal Behavior in SU(3) Yang-Mills Theories*, *Phys. Rev.* **D79** (2009) 076010, [arXiv:0901.3766].

[157] T. DeGrand and A. Hasenfratz, *Remarks on lattice gauge theories with infrared-attractive fixed points*, *Phys. Rev.* **D80** (2009) 034506, [arXiv:0906.1976].

[158] **ALPHA** Collaboration, M. Della Morte, R. Hoffmann, F. Knechtli, J. Rolf, R. Sommer, I. Wetzorke, and U. Wolff, *Non-perturbative quark mass renormalization in two-flavor QCD*, *Nucl. Phys.* **B729** (2005) 117–134, [hep-lat/0507035].

[159] L. Giusti and M. Luscher, *Chiral symmetry breaking and the Banks-Casher relation in lattice QCD with Wilson quarks*, *JHEP* **03** (2009) 013, [arXiv:0812.3638].

[160] A. Patella, *GMOR-like relation in IR-conformal gauge theories*, *Phys. Rev.* **D84** (2011) 125033, [arXiv:1106.3494].

[161] A. Cheng, A. Hasenfratz, G. Petropoulos, and D. Schaich, *Scale-dependent mass anomalous dimension from Dirac eigenmodes*, *JHEP* **07** (2013) 061, [arXiv:1301.1355].

[162] L. Del Debbio, L. Giusti, M. Luscher, R. Petronzio, and N. Tantalo, *Stability of lattice QCD simulations and the thermodynamic limit*, *JHEP* **02** (2006) 011, [hep-lat/0512021].

[163] A. Amato, V. Leino, K. Rummukainen, K. Tuominen, and S. Tähtinen, *From chiral symmetry breaking to conformality in SU(2) gauge theory*, arXiv:1806.07154.

[164] A. Hasenfratz, C. Rebbi, and O. Witzel, *Large scale separation and resonances within LHC range from a prototype BSM model*, *Phys. Lett.* **B773** (2017) 86–90, [arXiv:1609.01401].

[165] O. Antipin and F. Sannino, *Conformal Window 2.0: The large N_f safe story*, *Phys. Rev.* **D97** (2018), no. 11 116007, [arXiv:1709.02354].